Noname manuscript No.
(will be inserted by the editor)

Coupling of combustion simulation with atomisation and filming models for LES in swirled spray flames

Nicholas C. W. Treleaven · Davide Laera · Julien Carmona · Nicolas Odier · Yann Gentil · Jerome Dombard · Guillaume Daviller · Laurent Gicquel · Thierry Poinsot

Received: date / Accepted: date

Abstract High fidelity spray flame modelling without ad-hoc tuning of the injection parameters is proposed for an Euler-Lagrangian LES description of turbulent combustion in swirled two-phase flow chambers. It is tested in a laboratory burner (SICCA-Spray rig from EM2C), which comprises both a *simplex* pressure swirl and an airblast atomiser. Relevant phenomena controlling the liquid spray inside the injector including primary and edge atomisation from a pressure swirl and an airblast atomiser respectively, secondary atomisation, evaporation and the formation and dynamics of the liquid film that forms on the inner injector wall are taken into account. Particular attention has been applied to understanding the shape of the droplet diameter probability distribution function and how each atomisation model contributes to it. Results show excellent agreement of the spray statistics measured experimentally with and without combustion. A sensitivity analysis of the model parameters shows that the models are sufficiently insensitive to user chosen parameters, which, together with their relatively low computational cost, make these models ideal candidates for industrial applications.

Keywords LES · spray flame · two-phase flows · atomisation · liquid/wall interactions · turbulent spray flames · Eulerian-Lagrangian approach

This work was granted access to the HPC resources of IDRIS under the allocation 2022-[A0112B10157] made by GENCI. This project has received funding from the Clean Sky 2 Joint Undertaking (JU) under grant agreement No. 886554. The JU receives support from the European Union's Horizon 2020 research and innovation programme and the Clean Sky 2 JU members other than the Union.

Nicholas C. W. Treleaven, Davide Laera, Julien Carmona, Nicholas Odier, Yann Gentil, Jerome Dombard, Laurent Gicquel & Guillaume Daviller
CFD-Team, CERFACS
Toulouse, France
E-mail: treleaven@cerfacs.fr

Thierry Poinsot
IMFT
Toulouse, France

1 Introduction

The accurate prediction of swirl spray flames is important to improve the design of gas turbine combustion chambers that run on a variety of liquid fuels (diesel, kerosene, methanol, liquid ammonia, SAF (Sustainable Aviation Fuels) etc.). The greatest challenge in this field is the modeling of the liquid fuel atomisation processes. Direct numerical simulations of atomisation [1–3] and droplet interactions [4] are possible but require computational resources several orders of magnitude higher than those required for LES (Large Eddy Simulations) of single-phase turbulent swirl flames.

These restrictions have led to the use of simplified phenomenological models for spray atomisation, breakup and droplet interaction processes. The simplest option is to inject the fuel as a fully formed fuel spray outside of the injector using either Eulerian-Lagrangian or Eulerian-Eulerian methodologies [5–9] where the fuel spray parameters (Sauter mean diameter, diameter and velocity probability density functions) must be known before the simulation is run which necessitates the use of expensive and time-consuming experiments. This approach also suffers a lack of generality as a small change in the fuel injector design leads to a change in the gaseous phase flow field and therefore impacts the atomisation process too.

These problems become critical for airblast atomisers during combustion instabilities where the velocity and diameter statistics vary with time through the acoustic cycle [10]. Simulations show that changes in the droplet diameter distribution can lead to large fluctuations of heat release [11], and that the stability of a combustion chamber is dependent on the size of the film resting on the atomiser surface, which may become coupled to the oscillating airflow [12]. In [13], an Eulerian thin-film solution was calculated for the liquid film on the atomising edge that allows interaction between the liquid film and the airflow inside the injector. This solution was then used to provide an initial velocity condition for the atomised droplets. For some airblast atomisers, the atomiser is fed from a secondary fuel spray atomised by a pressure swirl atomiser. Under steady state conditions, the accuracy of the simulation is dependent on the proportion of fuel that strikes the atomiser walls and feeds the fuel film [14], while under thermoacoustically unsteady flow conditions, the cone angle of the spray produced by the pressure swirl atomiser varies and affects the stability of the combustion chamber [15].

A diagram of a fuel injector representative of aero-engines is shown in Fig. 1. This design reproduces the atomisation phenomena at laboratory scale in the SICCA-Spray injector from EM2C [14, 16–20] which includes both a pressure swirl and airblast atomiser producing two types of droplets (labeled Type 1 and Type 2 droplets respectively). Type 1 droplets undergo primary atomisation by the pressure swirl atomiser followed by secondary atomisation in the turbulent, swirling airflow. Type 2 droplets undergo a similar process but they also impact the injector walls where a liquid film is formed. This liquid film is then re-atomised at the injector lips of the airblast atomiser.

This study describes an attempt to use first-principle models for all two-phase flow mechanisms in a combustion chamber except for the initial primary atomisation created by the simplex atomiser. This requires a complete set of models for spray wall interaction, film, primary and secondary atomisation coupled to combustion: FIM-UR for atomisation at the pressure-swirl atomiser, FASTER for the secondary atomisation, FILM for the liquid film and PAMELA for re-atomisation

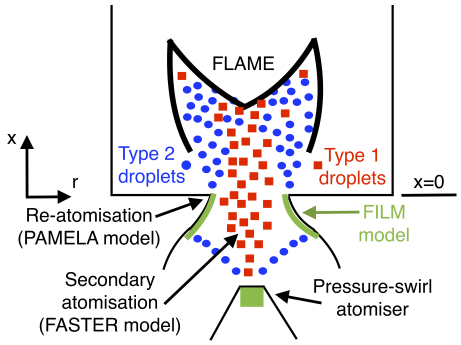

Fig. 1 A diagram showing the different physical phenomena present during the fuel atomisation process and the different models developed to handle each one.

at the injector lips. These models only require technical data provided with the atomiser. All models are used together to show how an accurate spray swirl flame can be modelled using LES. Furthermore, a sensitivity analysis of the input parameters is presented to highlight which parameters are important in reproducing the correct downstream spray statistics.

Section 2 presents the experimental rig. Section 3.1 describes the LES methodology for the gaseous phase followed by descriptions of the liquid spray models in Section 3.2. Finally, results are presented in Section 4, beginning with a comparison of the gaseous non-reacting flow with experiments (Section 4.1), followed by the spray simulation without combustion (Section 4.2) and finally the spray simulations with combustion (Section 4.3). Additional sections (Section 4.2.1, Appendix A and Appendix B) describe the effects of the swirling flow inside the injector on the spray dynamics, the sensitivity of the results to the choice of the models and the sensitivity of the models to the input parameters respectively.

2 The SICCA-Spray injector

The spray models introduced in this paper, have been tested in the SICCA-Spray rig of the EM2C laboratory at CentraleSupelec [14, 16–19]. It consists of a single fuel injector fed by an air swirler with a centrally located pressure swirl simplex atomiser (Fig.2a). For non-reacting cases, the fuel injector discharges directly into the atmosphere. For the reacting cases, a quartz tube is installed to mimic a combustion chamber. Flow, flame and spray measurements have been undertaken using laser and optical diagnostic techniques such as LDV (Laser Doppler Velocimetry), PIV (Particle Image Velocimetry), Mie scattering and PDA (Phase Doppler Anemometry) [16, 17, 14].

The air swirler can be easily changed to test different designs (Fig.2c-d). It promotes a swirling turbulent flow with a central recirculation zone and an M-shaped flame. The swirler used in this study is referred to as *S716* in [20] with a pressure drop of 5.74 kPa and a swirl number of 0.7. Experimental results are presented for this swirler in [14, 20]. It is different from the swirlers presented in other studies of the SICCA-Spray rig [12, 15, 16]. The pressure-swirl atomiser produces a fuel spray in a hollow cone pattern. Some of the spray is ejected directly

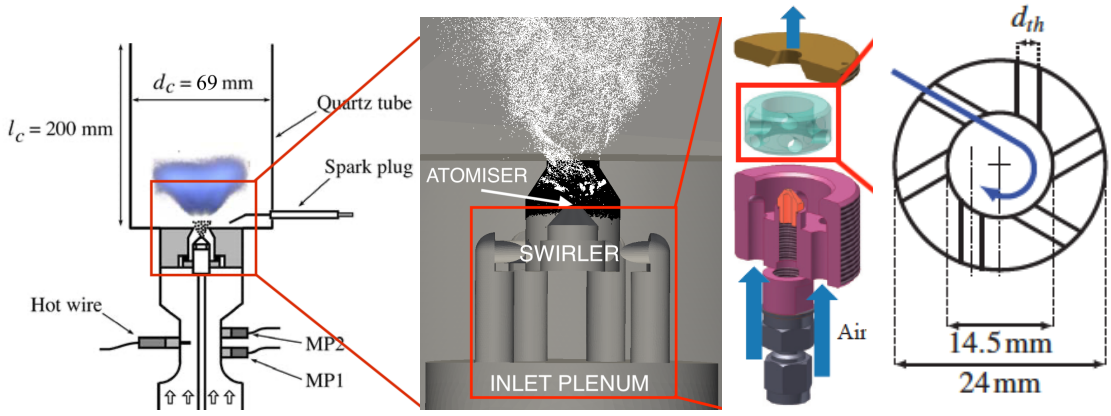

Fig. 2 (a) The SICCA-Spray experimental setup [16], (b) A cross-section of the injector showing the air swirler and the position of the pressure swirl atomiser. Atomised droplets are shown in white while the liquid film is shown in black for the non-reacting LES simulations. (c) Exploded view of the SICCA-Spray injector [24]. (d) Schematic of the air swirler [24].

into the combustion chamber while some of the fuel spray first makes contact with the inner surface of the injector where a fuel film is formed (Fig.2b). This film is then pulled downstream by the airflow to the ring formed at the point where the injector meets the combustion chamber backplane. This junction forms the atomising edge of an airblast atomiser where the fuel from the film is atomised into the combustion chamber.

3 Numerical methodology

3.1 Gaseous phase

All LES are computed using the *AVBP* solver (https://www.cerfacs.fr/avbp7x/) [25–27] . It is massively parallel, explicit in time and solves the compressible multi-species Navier-Stokes equations. Convective fluxes are solved using the Two-Step-Taylor-Galerkin C (TTGC) finite element scheme [28] whilst diffusive fluxes are solved using the 2Δ diffusion operator [29]. The code is third-order accurate in space and time. Turbulence closure is provided for through use of the WALE (Wall-Adapting Local Eddy-viscosity) subgrid scale model [30].

A cut through the computational domain for both reacting and non-reacting cases is shown in Fig. 3, which also displays the relevant boundary conditions. In both cases air is injected into the upstream plenum at a rate of 2.6 g/s using a NSCBC (Navier-Stokes Characteristic Boundary Condition) [31]. A no-slip velocity boundary condition is used for all walls except for inside the injector body where a log-law wall function is used. For the reacting simulations, a fixed temperature is imposed for the combustion chamber backplane with a temperature

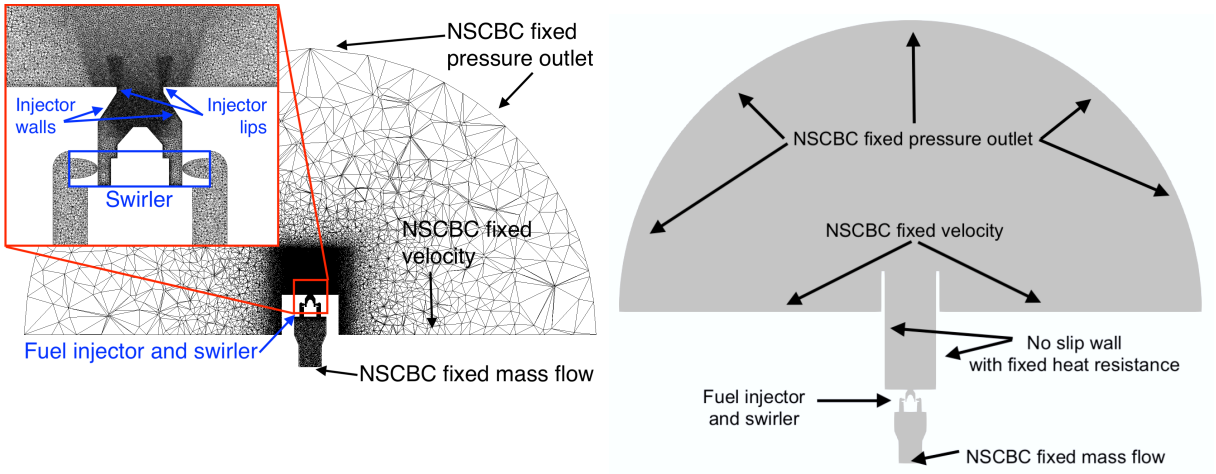

(a) Non-reacting domain (b) Reacting domain

Fig. 3 A cut plane through the computational domains highlighting the mesh and boundary conditions used.

of $T_{\mathrm{bkpl}} = 450$ K as measured in experiments. For the injector walls the outside temperature was set to $T_{\mathrm{inj}} = 420$ K as approximated during experiments, while the swirler walls were set to an outside temperature of $T_{\mathrm{sw}} = 370$ K as approximated in experiments. Following previous studies [12], for the chamber walls, an experimentally determined temperature profile was applied. In both reacting and non-reacting simulations the flow is discharged into a large hemispherical plenum whose curved surface is fitted with a NSCBC [32] outlet boundary condition where static pressure is relaxed towards $p_{\mathrm{out}} = 101325$ Pa. On the upstream side of the exit plenum a small coflow inlet velocity is applied to mimic air entrainment.

The computational domain is meshed using tetrahedral elements. In the flame stabilisation zone, the mesh size increases from between 0.24 mm to 0.6 mm and in the vicinity of the injector lips (Fig. 3a), it decreases to 0.11 mm. At the walls of the injector, it goes to 0.1 mm to capture the boundary layers leading to y^+ values of the order of 50-100 wall units, which justifies the use of a law of the wall boundary condition on these surfaces. The mesh is also refined on the surface of the combustor backplane to 0.22 mm and near the combustion chamber wall where it is set to 0.45 mm.

3.1.1 Combustion modelling

For the reacting case, kinetics are described using a reduced reaction scheme for heptane, comprising 6 species and 2 reactions [33]. A pre-exponential adjustment (PEA) upon local equivalence ratio is added to reproduce the correct laminar flame speed for rich mixtures. To account for subgrid scale turbulence-chemistry interaction, the classical DTFLES (Dynamic Thickened Flame Large Eddy Simulation) model [34] with the Charlette efficiency function [35] is used. Being a not fully premixed flame, the Takeno index [36] is used to deactivate thickening of diffusion flame regions.

3.2 Liquid Phase

For the liquid fuel spray phase, the Eulerian-Lagrangian formulation is used where the fuel spray is represented using a number of numerical parcels, each of which represents a number of spray droplets that share the same physical properties (location, velocity, temperature, mass, composition). At each time step the source terms for each parcel are calculated (drag forces, heat and mass transfer) and the state of each parcel integrated explicitly in time. The source terms are also applied to the Navier-Stokes equations governing the gaseous phase to ensure that the effect of the fuel spray is felt by the gas flow [12].

The Abramzon and Sirignano model [37] assuming constant evaporation Prandtl and Schmidt numbers [38] is used for evaporation. For n-heptane these have been fixed to $\mathrm{Pr_{ev}} = 0.976$ and $\mathrm{Sc_{ev}} = 1.343$ respectively [12]. Drag forces are computed using the correlation of Naumann and Schiller [39]. When interacting with the thickened flame the rate of evaporation and the amount of drag experienced by the particles is augmented. The two-phase extension of the DTFLES model (TP-TFLES) model [40] is used that divides the source terms by the thickening factor to preserve the ratios between the evaporation, droplet relaxation and chemical timescales.

To model the atomisation processes in turbulent swirl spray flames, multiple numerical models are required (Fig.1): 1. atomisation from the pressure-swirl atomiser (Laminar FIM-UR); 2. formation and propagation of the liquid film on the injector wall (FILM); 3. atomisation from the airblast atomiser (Automatic PAMELA); and 4. secondary breakup of atomised droplets (FASTER). Each model is presented hereafter.

3.2.1 Laminar FIM-UR

The FIM-UR (Fuel Injection Method by Upstream Reconstruction) model [9] is used to inject Lagrangian parcels in a hollow cone spray pattern with a mean half cone angle of θ_S from a ring with inner radius R_a and outer radius R_0. The inner diameter corresponds to the diameter of the air core that forms along the centreline of the swirling flow inside the atomiser (Fig. 4a). It is calculated using the empirical formula of Rizk and Lefebvre [41]:

$$\frac{A_{\mathrm{air}}}{A_{exit}} = \left(\frac{R_a}{R_0}\right)^2 = \frac{\sin^2(\theta_S)}{1+\cos^2(\theta_S)} \tag{1}$$

It is assumed that the droplets released with an angle of θ_S are injected at the midpoint between R_a and R_0 (Fig. 4b). Assuming that the trajectories of all droplets are coincident at a point x_0 behind the plane of injection allows for an equation to be developed that links the radial position of the injection to the angle of injection. Taking the outer radius of the injector as the radius of injection results in the highest angle of injection:

$$\tan(\theta_{\max}) = \frac{2R_0\tan(\theta_S)}{R_0+R_a} \tag{2}$$

In the SICCA-Spray rig, the fuel spray coming from the pressure-swirl atomiser undergoes a so-called *explosive breakup* process [14] that makes it difficult to define

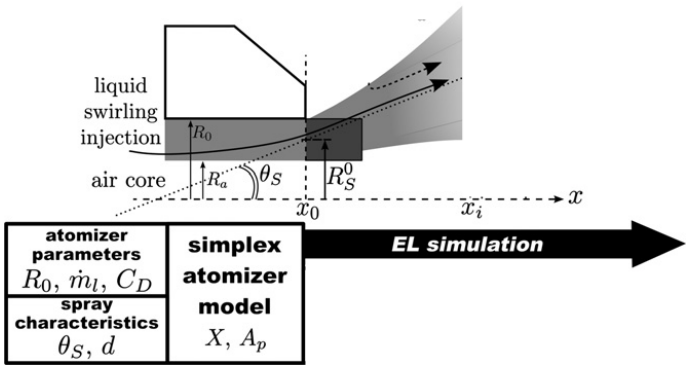

(a) Schematic of the FIM-UR model [9].

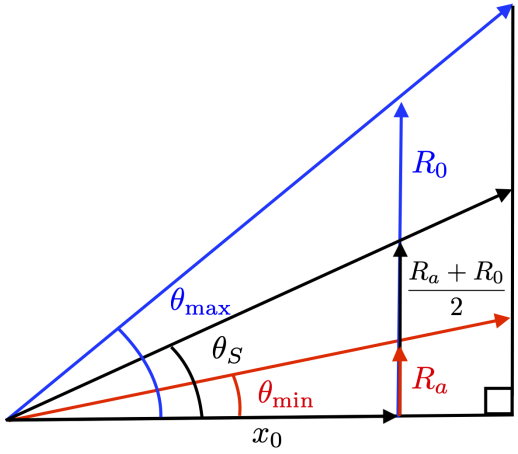

(b) Diagram showing the maximum and minimum (in the original FIM-UR model) spray angles.

Fig. 4 The FIM-UR model for the simplex atomiser.

a mean half cone angle and broadens the thickness of the spray cone. As proposed in [14], the broadening of the spray cone is captured by injecting droplets at an angle randomly selected from a normal distribution with a fixed mean and standard deviation. In the proposed version, the minimum spray angle ($\theta_{\min}$), differently from the original FIM-UR model, is considered as an additional input parameter. For the analysed SICCA-Spray case an optimised mean and minimum angle of $\theta_S = 65$ degrees and $\theta_{\min} = 10$ degrees respectively have been chosen with an atomiser radius of the atomiser (R_0) of 50 microns.

In the original FIM-UR model the axial velocity of all injected droplets is set to the bulk velocity of the fluid passing through the orifice:

$$U_p = \frac{\dot{m}_p}{\rho_p \pi (R_0^2 - R_a^2)} \tag{3}$$

However, a radius of R_0 corresponds to the wall of the atomiser where the velocity must be zero. Similarly at a radius of R_a, the mean axial velocity must be zero because there is no net flow of air out of the atomiser. Although the flow inside the upstream swirl chamber is turbulent, the rapid acceleration of the fluid through the orifice and small length of the orifice means that the velocity profile is more likely to be laminar (parabolic). Following these considerations, in the newly proposed Laminar FIM-UR model, the velocity profile is prescribed as a function of the radius r:

$$u_{x,p}(r) = a(r^2 - r(R_0 + R_a) + R_0 R_a) \tag{4}$$

for $R_a < r < R_0$, with:

$$a = \frac{U_p R_2}{2(R_4/4 - R_3(R_0 + R_a)/3 + R_2 R_0 R_a/2)} \tag{5}$$

where U_p is the bulk velocity in Eqn. (3) and:

$$R_4 = R_0^4 - R_a^4,\ R_3 = R_0^3 - R_a^3,\ R_2 = R_0^2 - R_a^2 \tag{6}$$

As in the original FIM-UR model, the fuel is bounded by the wall of the orifice at the point of atomisation and at a radius of R_0: this has the effect of constraining the radial velocity to zero. In order to obtain the required cone angle, the tangential velocity of the droplets is set to:

$$\overline{u}_\theta = \overline{u}_x \tan(\theta) \tag{7}$$

Finally, the droplets exhibit a certain level of stochastic variation, so that the velocities are modified to become:

$$u_{x,p} = \overline{u}_{x,p} + r_1 \sigma_u \tag{8}$$

$$\overline{u}_{r,p} = r_2 \sigma_u \tag{9}$$

$$\overline{u}_{\theta,p} = \overline{u}_x \tan(\theta) + r_3 \sigma_u \tag{10}$$

where σ_u is the desired level of stochastic variation in the velocity and r_1, r_2, r_3 are random numbers in the interval of [-1,1]. An additional random number generator is used to choose an injection angle θ that lies between the minimum $\theta_{\min}$ and maximum $\theta_{\max}$ spray cone angles and a radius that lies between R_a and R_0. The injection velocity is then found using Eqns. 3-10.

In order to choose the diameter of the injected droplets both a Rosin-Rammler (RR) and modified Rosin-Rammler (MRR) distribution have been tested. The cumulative distribution of the RR distribution is given by:

$$1 - Q(d_p) = \exp(-(d_p/X)^q) \tag{11}$$

whilst for the MRR it is:

$$1 - Q(d_p) = \exp(-(\ln(d_p)/\ln(X))^q) \tag{12}$$

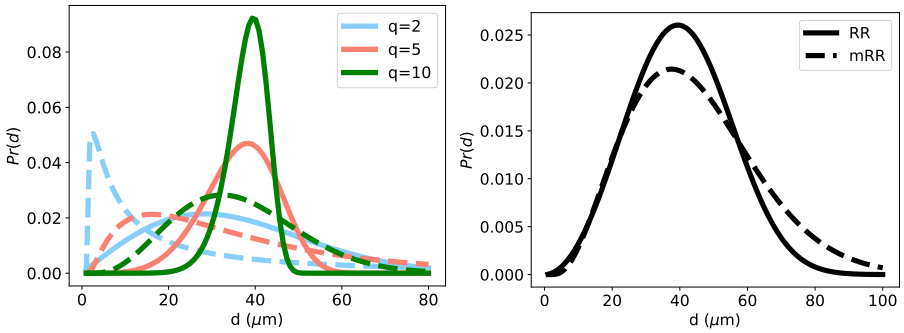

(a) (b)

Fig. 5 The RR (solid line) and MRR (dashed line) distributions for $X = 40$ microns for various spreading parameters (a) and the result of fitting the MRR to the RR distribution (b).

where X is a scale parameter, q is a spreading parameter and Q is the proportion of droplets smaller than d_p in the distribution. In the case of the RR distribution, the scale parameter (X) can be linked to the SMD (D_{32}) through [42]:

$$D_{32} = \frac{X\Gamma\left(\frac{3}{q}+1\right)}{\Gamma\left(\frac{2}{q}+1\right)} \tag{13}$$

where Γ is the gamma function. Unfortunately a similar expression does not exist for the MRR distribution which makes the distribution more difficult to use as the droplet SMD is often included in the specifications of a certain atomiser nozzle. Nevertheless the MRR distribution better represents the largest droplets in the distribution [43]. Although there may be a small number of these large droplets, they contain a non-negligible quantity of fuel. Because of their greater size they take longer to evaporate, penetrating further into the combustion chamber.

In this study, the SMD (D_{32}) and spreading parameter (q) were unknown. The solution is not overly sensitive to the choice of X and q providing that: (a) the distribution contains very few droplets less than 10 microns and; (b) that the distribution is sufficiently broad to represent the largest droplets (which implies use of the MRR distribution in preference to the RR distribution). This is because (a) the smallest droplets are least likely to deposit on the walls of the injector and hence dominate the droplet distribution downstream; (b) the secondary breakup model can break large droplets into smaller ones but cannot account for agglomerations of smaller droplets; and (c) the downstream distribution is dominated by the secondary breakup process which is relatively insensitive to the size of the input droplets [44]. The sensitivity of the results to the choice of distribution is demonstrated in Appendix A. After an optimisation of the droplet distribution in order to match the experimental results under both reacting and non-reacting conditions, an SMD of 50 microns was selected and a RR distribution generated that resembled a close to Gaussian shape. In this study, in order to convert the RR distribution into an equivalent MRR distribution, the equivalent MRR distribution was generated by performing a best fit operation over the first 25% of diameters.

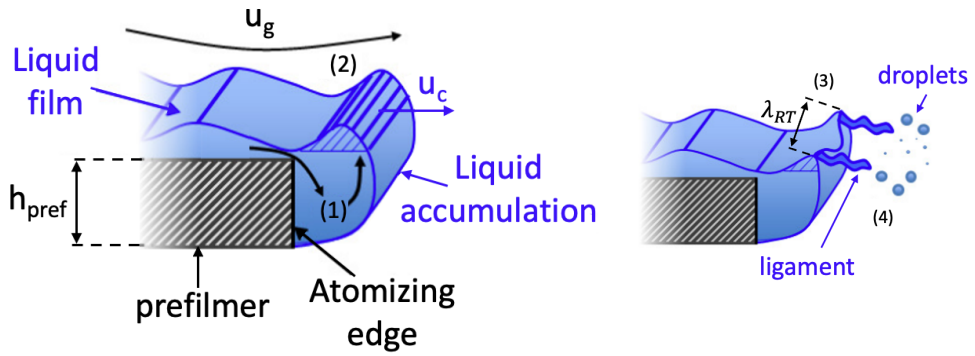

(a) The accumulation of the fuel at the prefilming edge.

(b) The formation of ligaments and the breakup into droplets .

Fig. 6 The two main steps used to model the atomisation process for airblast atomisers ([23]).

The final distribution is shown in Fig. 5 which was obtained with $X = 52.19$ microns and $q = 8.87$.

3.2.2 FILM

If a Lagrangian particle impacts the inner surface of the injector, it is assumed to form part of a liquid film that grows on the surface and moves downstream to the airblast atomiser edge. Particles entrapped in the film move according to a local cell average velocity calculated using the Saint-Venant equations [45,46,22]. The height of the film in each cell is calculated from the total volume of fuel droplets and the surface area of the atomiser surface lying in each cell.

3.2.3 Automatic PAMELA

When the liquid film reaches the injector lip, it is atomised into Lagrangian particles via the Automatic-PAMELA (Primary Atomisation Model for prEfilming airbLAst injectors) model. This model, originally developed by Chaussonnet et al. [47,23], then improved by Carmona et al. [48,49] allows the re-atomisation of the liquid droplets in the film in a realistic way based on local flow information, local liquid film information and the atomiser geometry information. It is based on a set of correlations established and calibrated from the experiments of Gepperth et al. [50] by Chaussonnet et al. [47,23]. The model assumes that the film atomisation process occurs following 4 steps (Fig. 6): (1) The liquid feeds a reservoir located at injector lip. (2) Due to the surrounding high-speed gas flow, a part of the liquid contained in the reservoir is sheared and accelerated downstream of the injector. (3) A Rayleigh-Taylor instability develops over the liquid reservoir surface in the spanwise direction. (4) This instability is ripped off by the high-speed air stream into bags and ligaments that quickly disintegrate into a spray. The droplet diameter distribution of the generated spray is assumed to follow a Rosin-Rammler cumulative distribution function (CDF):

$$1 - Q(d_p) = \exp(-(d_p/X)^q) \tag{14}$$

The SMD (D_{32}) is assumed to be related to the characteristic Rayleigh-Taylor instability wavelength (λ_{RT}) at the atomiser edge:

$$D_{32} = C_2 \lambda_{RT} \tag{15}$$

and together with Eqn. 13, this becomes:

$$X = C_2 \, \lambda_{RT} \, \frac{\Gamma(2/q+1)}{\Gamma(3/q+1)} \tag{16}$$

where Γ refers to the Gamma function and C_2 is a model constant. The Rayleigh Taylor instability wavelength (λ_{RT}) is estimated from:

$$\lambda_{RT} = \frac{2\pi}{r_\rho u_g} \sqrt{\frac{6 \, C_1 \, h_{\text{pref}} \, \sigma}{\rho_g}} \tag{17}$$

where C_1 is a model constant, h_{pref} is the prefilmer height, σ is the liquid surface tension, u_g is the gas velocity and r_ρ is a ratio of the liquid (ρ_l) and gas (ρ_g) densities defined as:

$$r_\rho = \frac{\sqrt{\rho_l}}{\sqrt{\rho_l} + \sqrt{\rho_g}} \tag{18}$$

Equation 16 can be recast into a practical relation that directly links X with the surrounding flow characteristics:

$$X = C_{12} \frac{h_{\text{pref}}}{\sqrt{\text{We}_{\text{pref}}}} \frac{\Gamma(2/q+1)}{\Gamma(3/q+1)} \tag{19}$$

where $C_{12} = 2\pi \, C_2 \, \sqrt{6 \, C_1}$ is a model constant and We_{pref} is a Weber number based on the thickness of the prefilmer:

$$\text{We}_{\text{pref}} = \frac{\rho_g \, h_{\text{pref}} \, (r_\rho u_g)^2}{\sigma} \tag{20}$$

The shape parameter q is determined using:

$$q = \frac{C_3}{\sqrt{\text{We}_\delta}} + g(h_{\text{pref}}) \tag{21}$$

This equation has been established from the analysis of experimental CDFs by [23] and involves an other model constant C_3 and a Weber number based on the gaseous boundary layer thickness (δ_g):

$$\text{We}_\delta = \frac{\rho_g \, u_g^2 \, \delta_g}{\sigma} \tag{22}$$

$g(h_{\text{pref}})$ is related to the prefilmer thickness through:

$$g(h_{\text{pref}}) = \left(\frac{C_4}{h_{\text{pref}}} \right)^2 + C_5 \tag{23}$$

with C_4 and C_5 also being model constants. All constants C_1, C_2, C_{12}, C_3, C_4 and C_5 have been tuned during a calibration process described in [48,49] (Tab.

1). In many cases, the airblast atomiser thickness (h_{pref}) is linked explicitly to the geometry, however in the case of the SICCA-Spray rig, the atomiser is formed by the join of two edges without a defined thickness. The value of h_{pref} is therefore a free parameter in the case of an edge atomiser such as the one in the SICCA-Spray rig. In this study it was set to $h_{\text{pref}} = 1$ mm to best agree with reacting and non-reacting experimental data.

C_1	C_2	C_{12}	C_3	C_4	C_5
0.381	0.112	1.0643	5.13	4.29 mm	$-1.68 \cdot 10^{-1}$

Table 1 Calibrations constants of the Automatic-PAMELA model established in [48,49].

The time scale of the atomisation process τ_{tot} is expressed as the sum of the Rayleigh-Taylor instability time scale τ_{RT} and the breakup time scale τ_{bu}. Both are proportional to a capillary time scale τ_c [23]:

$$\tau_{RT} = 10\,\tau_c \tag{24}$$

$$\tau_{bu} = 1.8\,\tau_c \tag{25}$$

where the capillary time scale is estimated by the following equation:

$$\tau_c = \left(\frac{\sigma}{a^3|\rho_l - \rho_g|}\right)^{1/4} \tag{26}$$

with the acceleration of the instability crest given by:

$$a = \frac{1}{2}\frac{1}{C_1\,h_{pref}}\frac{\rho_g}{\rho_l}(r_p u_g)^2 \tag{27}$$

The characteristic time scale τ_{tot} is finally expressed as the sum of time τ_{RT} and τ_{bu}:

$$\tau_{tot} = 11.8\,\tau_c \tag{28}$$

The gas velocity seen by the liquid film (u_g) and the gaseous boundary layer thickness (δ_g) must be locally estimated. The Automatic-PAMELA model [48,49] computes the gas velocity assuming a logarithmic velocity profile:

$$u_g = u_\tau\left[\frac{1}{\kappa}\ln(h_f^+) + B\right] \tag{29}$$

with $B = 5.41$, $\kappa = 0.41$ and h_f^+ is the film height expressed in wall units:

$$h_f^+ = \frac{h_f u_\tau}{\nu_g} \tag{30}$$

and u_τ is the friction velocity calculated thanks to the wall shear stress τ_w at the atomising edge,

$$u_\tau = \sqrt{\frac{\tau_w}{\rho_g}} \tag{31}$$

Finally, δ_g in Eqn.(22) is defined as the distance from the wall where the local velocity exceeds 99% of the bulk velocity.

3.2.4 FASTER

Secondary atomisation occurs in the free-stream and after primary atomisation as modelled using the FIM-UR or PAMELA models. The model for the secondary atomisation of droplets (Fig.1) is called FASTER (Fast Atomisation Stochastic Treatment wEber ohnesoRge). Based on the FAST (Fast Atomisation Stochastic Treatment) approach [21], FASTER assumes that the breakup of droplets occurs similarly to Kolmogorov's discrete model of solid particle-breakup [51] i.e. that each breakup event is statistically independent. Apte et al. [44] showed that Kolmogorov's model, in the long-time limit, could be rewritten in the form of a differential Fokker-Planck equation where the log-normal probability distribution of child droplets depends only on the first two moments of the distribution ($\langle\xi\rangle, \langle\xi^2\rangle$):

$$f(r_c,t) = \frac{1}{r_c}\int_0^\infty \frac{1}{\sqrt{2\pi\langle\xi^2\rangle\nu t}}\exp\left[\frac{-(\log(r_p/r_c)+\langle\xi\rangle\nu t)^2}{2\langle\xi^2\rangle\nu t}\right] f_0(r_p)\mathrm{d}r_p \quad (32)$$

where ν is the breakup frequency, f_0 is the parent droplet distribution, r_c is the radius of the child droplet, r_p is the radius of the parent droplet and t is the time. In the case of a single parent droplet undergoing breakup, f_0 is reduced to a delta function and $\nu t = 1$ leading to a cumulative distribution function ($T(r_c)$):

$$T(r_c) = \left[\frac{1}{2} + \frac{1}{2}\mathrm{erf}\left(\frac{\ln(r_c) - \ln(r_p) - \langle\xi\rangle}{\sqrt{2\langle\xi^2\rangle}}\right)\right] \quad (33)$$

It was observed in [52] and [53] that the breakup of sprays exhibits a fractal like behaviour that implies a lack of preferential scale. As this property closely resembles the turbulent energy cascade, Apte et al. [44] assume that $u_r^3/d_p \sim u_{r,cr}^3/d_{cr}$ (cr represents the critical values above which, breakup occurs) leading to:

$$\langle\xi\rangle = k_1 \log\left(\frac{\mathrm{We}_{cr}}{\mathrm{We}}\right) \quad (34)$$

where We= $\rho_g d_p u_r^2/\sigma_l$ is the Weber number, We_{cr} is the critical Weber number with a critical droplet diameter d_{cr} (above which, a droplet will breakup), k_1 is a constant with a value around unity (set to $k_1 = 0.8$ in this study), d_p is the diameter of the parent droplet, σ_l is the liquid surface tension, ρ_g is the density of the surrounding gas and u_r is the relative velocity between the droplet and the surrounding air. For the second moment $\langle\xi^2\rangle$, Apte et al. [44] argue that as the diffusion coefficient in the Fokker-Planck equation is related to the energy of Brownian motion, this energy is analogous to the disruptive energy that seeks to break up the parent droplet and that the ratio of this energy to the capillary force on the droplet is represented by the maximum stable droplet diameter d_{cr}. This leads to an equation for the second moment of the distribution:

$$-\frac{\langle\xi\rangle}{\langle\xi^2\rangle} = k_2 \log\left(\frac{d_p}{d_{cr}}\right) \quad (35)$$

where k_2 is also a constant close to unity (set to $k_2 = 1.2$ in this study). The parameter d_{cr} is provided thanks to the evaluation of a critical Weber number

$We_{cr} = \rho_g d_{cr} u_r^2/\sigma_l$ that can be approximated using the correlation of Brodkey [54]:

$$We_{cr} = 12(1 + 1.077\mathrm{Oh}^{1.6}) \tag{36}$$

where Oh$= \mu_l/(\rho_l d_p \sigma_l)^{0.5}$ is the Ohnesorge number and μ_l is the liquid viscosity. Droplets with a Weber number higher than the critical Weber number are assumed to breakup into smaller droplets.

Droplet breakup however, is not an instantaneous process. Three important timescales control droplet breakup [55]: (1) the time until initiation of breakup, (2) the time until primary breakup and, (3) the time until total breakup. The first time is defined as the point where breakup begins, the second is when the original droplet is no longer distinguishable and the third is when the breakup process is complete. For the FAST and FASTER models, there is no distiction between these events i.e. breakup happens at a time t_{bu} and is completed within one time step. This breakup time can be non-dimensionalised to yield a dimensionless characteristic breakup time T:

$$t_{bu} = T\sqrt{\frac{\rho_l}{\rho_g}}\frac{d_p}{u_r} \tag{37}$$

In the FAST model, TAB (Taylor Analogy Breakup) [56] and the model of Apte et al. [44], the breakup time t_{bu} is defined as:

$$t_{bu} = B\sqrt{\frac{\rho_l}{\rho_g}}\frac{r_p}{u_r} \tag{38}$$

where B is a non-dimensional coefficient that, based on a theoretical anaylsis of the time required for the breakup of a spherical particle, is set to $B = \sqrt{3}$ [56]. However, B is often used as a tuneable parameter to improve the agreement of simulations with experimental data [57]. Comparing Equations (37) and (38), it is clear that $B = 2T$. It should be noted that in [56] it is clearly stated that $B = \sqrt{3}$ is appropriate for high Weber numbers. In Pilch and Erdman [55], the characteristic time until primary breakup is given as $T = 1.25$ for We$>$ 350 based on experimental observation. The theoretical value of $B = \sqrt{3} \approx 1.73$ from [56] is close to the experimentally determined $B = 2T = 2.5$ and either of these numbers therefore seem reasonable for high Weber number (and low Ohnesorge number) cases. Unfortunately, in the case of SICCA-Spray, the Weber number is often significantly lower than 350. In [55], an additional correlation is given for the time until initiation of breakup (T_{in}) based on experimental observation:

$$T_{\mathrm{in}} = 1.9(\mathrm{We} - 12)^{-0.25}(1 + 2.2\mathrm{Oh}^{1.6}) \tag{39}$$

Figure 7 shows Eqn.(39) with $B = 2T = 2T_{\mathrm{in}}$ plotted for different Weber and Ohnesorge numbers including a typical Ohnesorge number for the SICCA-Spray rig (Oh$=$ 0.012). It also shows a typical Weber number for the SICCA-Spray rig ($u_r = 60$ m/s, $d_p = 80$ microns, We$=$ 18) and the value $B = 1.73$, as given by the TAB model. For low Weber numbers (We$<$ 35), using $B = 1.73$ results in breakup times that are too low (Fig. 7) because primary breakup should not occur before initiation of breakup. The FASTER model uses the definition for the time until breakup given by Eqns.(39) & (37) that also ensures that the model can be used

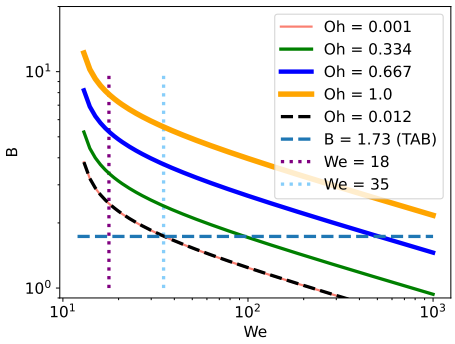

Fig. 7 The breakup coefficient B as given by the TAB model ($B = 1.73$) [56,44] and for various different Ohnesorge numbers as given by Eqn.(39). A typical Weber number for the SICCA-Spray rig (We=18) is also reported.

in the case of high Ohnesorge numbers. In contrast, FAST uses $B = \sqrt{3}$ and Eqn.(38).

FASTER first compares the age of a droplet to the breakup time as calculated using Eq. (38) where $B = 2T_{\text{in}}$ and T_{in} is calculated using Eq. (39). The droplet diameter is then compared to the critical droplet diameter given by the critical Weber number in Eqn.(36). When the diameter exceeds this critical value and the time exceeds the breakup time, the droplet is transformed into a series of child droplets whose radii are computed from Eqn.(33). The child particles have the same properties as the parent except for their radius and velocity. Their velocity is calculated from two contributions, the first is the velocity from the parent and the second is a random tangential velocity component with the magnitude of:

$$|u_{bu}| = \frac{r_p}{t_{bu}} \tag{40}$$

This tangential velocity is imposed randomly in a plane normal to the relative velocity between the particle and the gas.

4 Results and discussion

4.1 Single Phase

The configuration was simulated first without fuel spray or combustion. Results were compared against LDV (Laser Doppler Velocimetry) measurements of the same configuration at EM2C, CentraleSupelec. Mesh independence was verified by using two meshes (M_1 and M_2) where the mesh size was reduced from 0.4 mm to 0.1 mm in the injector swirler passages. The mesh M_1 contains 24 million cells while M_2 contains 30 million cells. Mean velocity profiles are compared at three different planes downstream ($x = 2.5$ mm, $x = 5$ mm and $x = 10$ mm in Fig. 1) in Fig. 8. Across both meshes and across the three planes the results show excellent agreement except at the plane furthest downstream for the radial velocity, which is consistent with the results of [12,14].

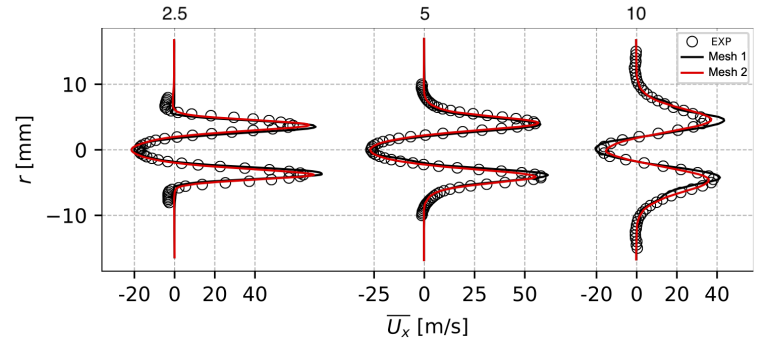

(a) Axial velocity

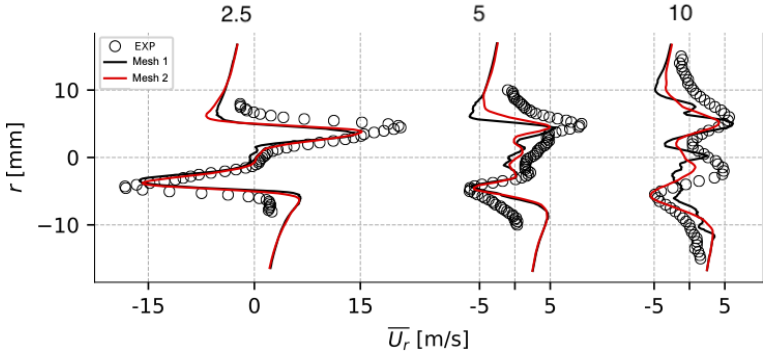

(b) Radial velocity

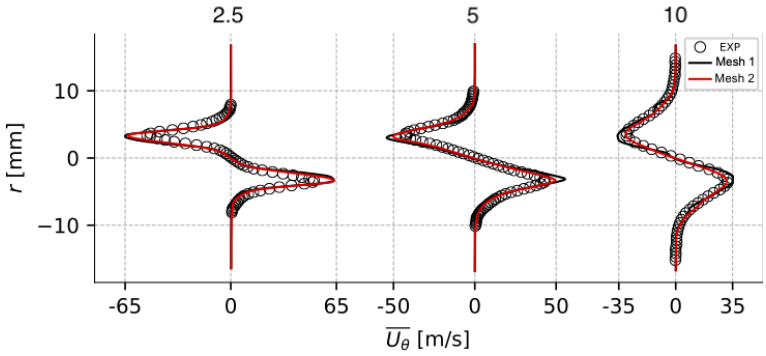

(c) Azimuthal velocity

Fig. 8 Mean velocity profiles measured by LDV in the experiment and the LES predictions using M_1 and M_2 at $x = 2.5$ mm, $x = 5$ mm and $x = 10$ mm in Fig. 1.

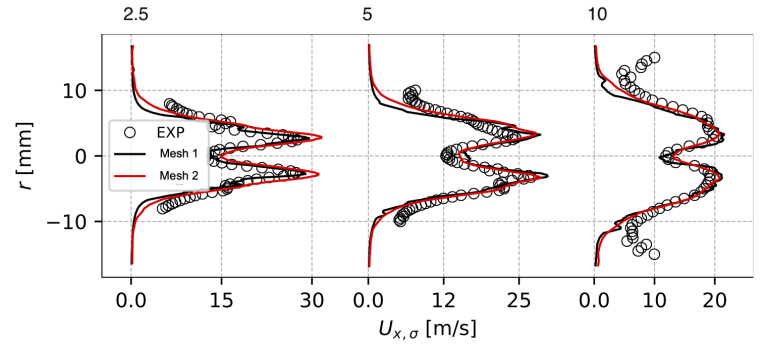

(a) Axial velocity

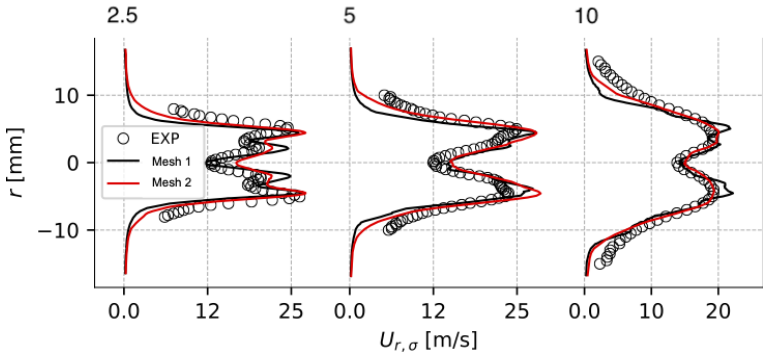

(b) Radial velocity

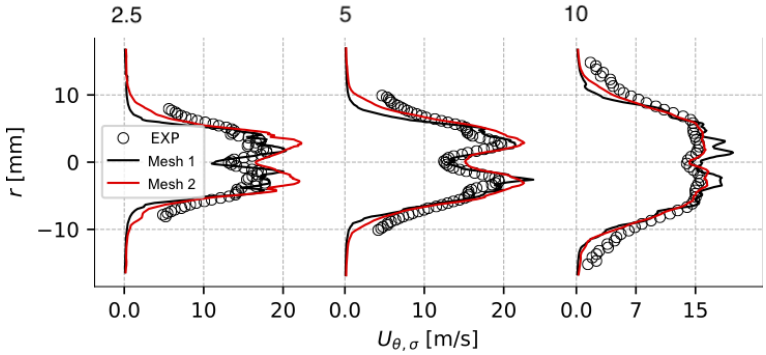

(c) Azimuthal velocity

Fig. 9 RMS velocity profiles as labelled in Fig.8.

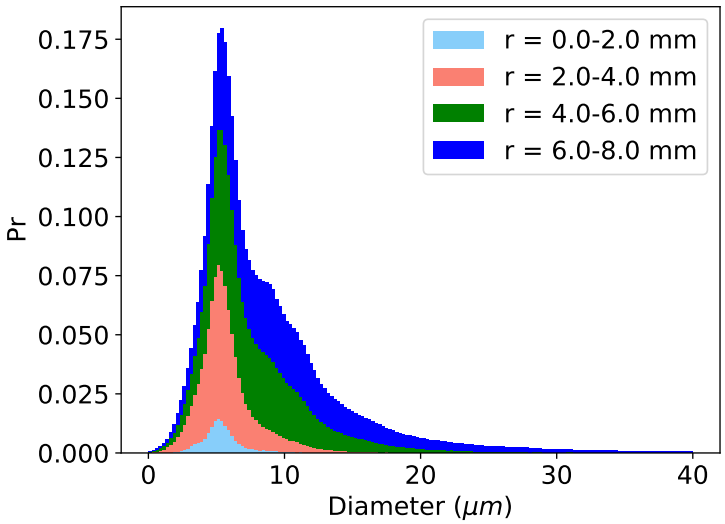

Fig. 10 The histogram for droplet diameter 5 mm downstream of the injector exit as measured in non-reacting experiments. This histogram has been coloured according to the radial measurement location of the collected droplets. The overall curve is the sum of all radial positions (0 to 8 mm)

Figure 9 shows the RMS of the mean velocity profiles from the two simulations and the experiment. The agreement between LES and experiment is extremely good. The largest errors are seen at far radial distances from the centreline of the injector. As the results for both meshes are similar, the mesh densities chosen for mesh M_1 were used in all simulations.

4.2 Fuel spray without combustion

Figure 10 shows the numerical histogram of the particle count for droplets measured 5 mm downstream of the injector exit plane in the experiments under isothermal conditions. The distribution can be thought of as being the superposition of two peaks: one at 6 microns and a second lower peak in the region of 7-10 microns. Figure 10 also shows the relative contribution that droplets make to this PDF (Probability Density Function) as a function of radial measurement location: droplets measured close to the centreline have a very small variation in their observed diameters with a mean at around 5 microns.

Numerical predictions are compared to experimental observations in two planes at x = 5 mm and 10 mm downstream from the injector lips (Fig.1). Figure 11 shows the histograms, droplet diameter profiles and axial velocity profiles for both simulations and experiments. The histograms are stacked, thereby showing the relative contributions of the droplets passing through the different models (FIM-UR, FASTER, PAMELA): a green colour indicates that the droplets present at this location were produced by secondary atomisation (FASTER) following primary atomisation by FIM-UR; the blue colour indicates droplets that have been produced by the secondary atomisation model (FASTER) after being released by

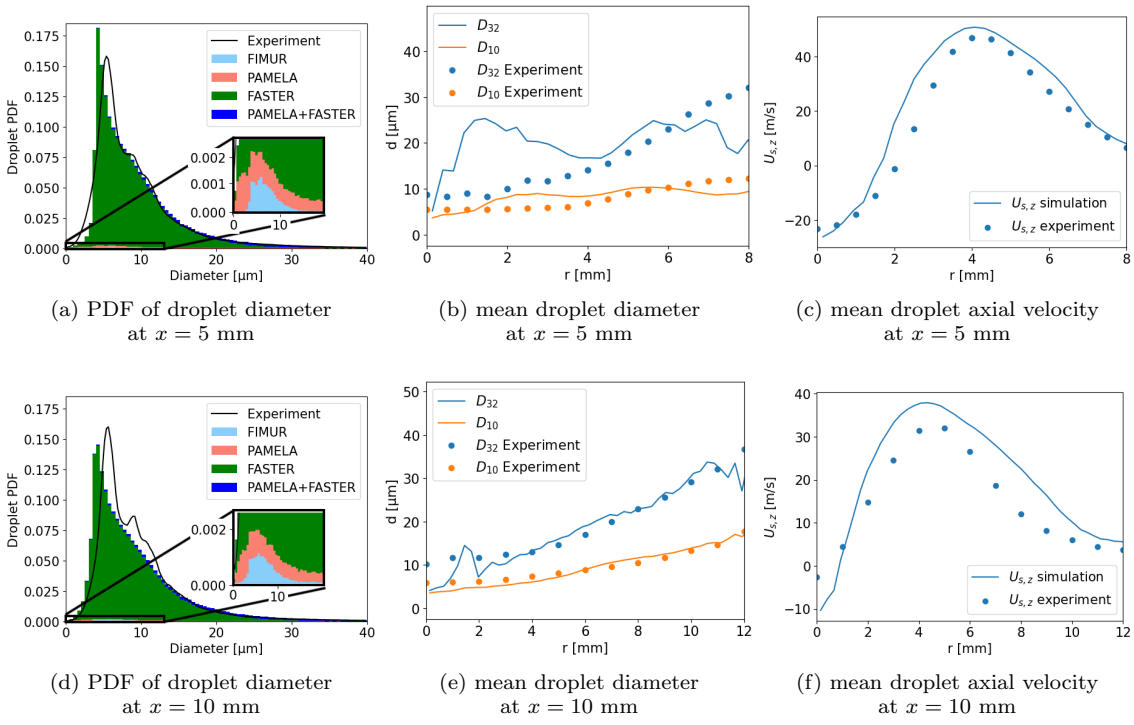

(a) PDF of droplet diameter at $x = 5$ mm

(b) mean droplet diameter at $x = 5$ mm

(c) mean droplet axial velocity at $x = 5$ mm

(d) PDF of droplet diameter at $x = 10$ mm

(e) mean droplet diameter at $x = 10$ mm

(f) mean droplet axial velocity at $x = 10$ mm

Fig. 11 Particle diameter probability, radial distribution and mean droplet axial velocity at $x = 5$ mm (a-b-c) and at $x = 10$ mm (d-e-f) (Fig.1) for the non-reacting simulation.

edge atomisation (PAMELA); cyan indicates FIM-UR released droplets observed in the measurement plane without undergoing additional atomisation; and salmon indicates droplets released by the edge atomising model (PAMELA) without subsequent secondary atomisation. It is noted that most droplets are generated by the secondary breakup model FASTER after primary atomisation without impacting the wall.

The droplet diameter profiles (Fig.11b and 11e) show very good agreement except for the SMD at 5 mm downstream indicating that there are too many large droplets at this point in the domain. However, 5 mm further downstream, this discrepancy vanishes, which indicates that the FASTER secondary breakup model does a good job of breaking up these droplets. The particle mean axial velocity profiles (Fig.11c and 11f) show excellent agreement except close to the centreline where the velocity is slightly too low for the measurements made 10 mm downstream and slightly too high further radially outwards (Fig.11f).

The quality of LES for two-phase flows can be checked by considering droplet velocity-size correlations. Figures 12 and 14 show a set of two-dimensional histograms giving the probability of a droplet of a certain diameter possessing a certain axial velocity at $x = 5$ mm and $x = 10$ mm (Fig.13). Results are presented for both experiment (a,b,c) and simulation (d,e,f) taken at different radial locations (r=3,5 and 7 mm in Fig.13). Droplets at a radial distance of 5 mm have

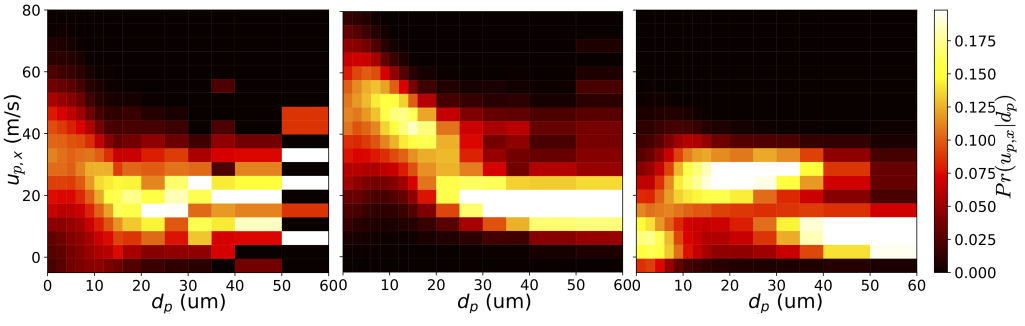

(a) At $r = 3$ mm for the experiment (b) At $r = 5$ mm for the experiment (c) At $r = 7$ mm for the experiment

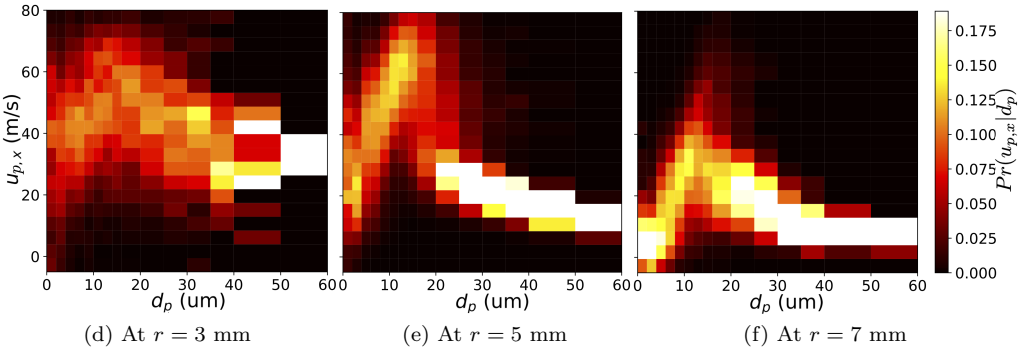

(d) At $r = 3$ mm for the simulation (e) At $r = 5$ mm for the simulation (f) At $r = 7$ mm for the simulation

Fig. 12 The probability of droplets having a certain axial velocity ($u_{p,x}$), conditioned by their diameter as measured $x = 5$ mm downstream of the exit of the injector (Fig. 1).

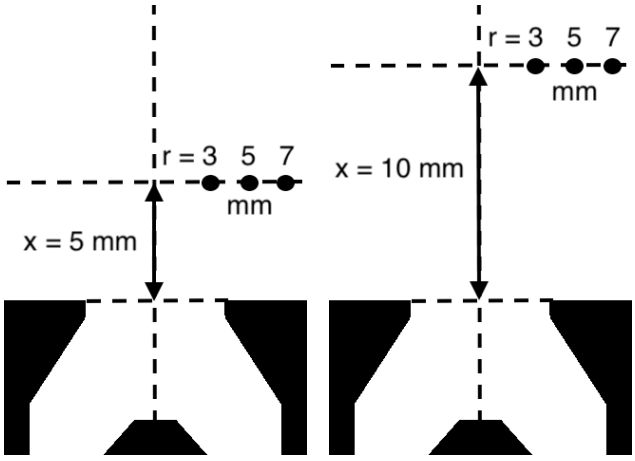

(a) (b)

Fig. 13 The location of the probes for measuring the velocity-diameter joint PDFs at $x = 5$ mm (a) and $x = 10$ mm (b).

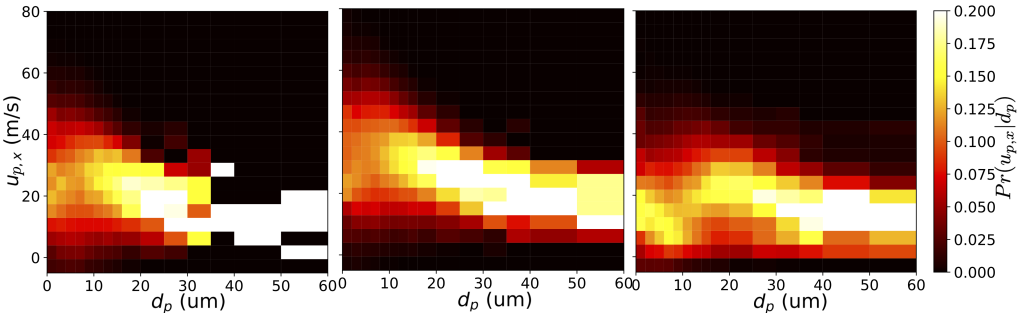

(a) At $r = 3$ mm for the experiment (b) At $r = 5$ mm for the experiment (c) At $r = 7$ mm for the experiment

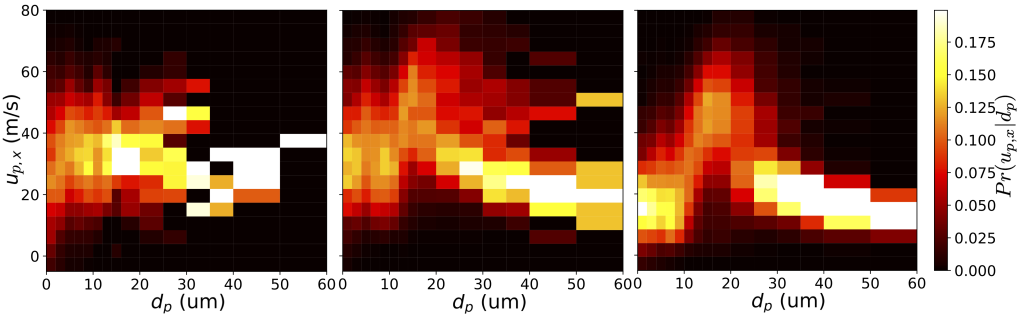

(d) At $r = 3$ mm for the simulation (e) At $r = 5$ mm for the simulation (f) At $r = 7$ mm for the simulation

Fig. 14 The probability of droplets having a certain axial velocity ($u_{p,x}$), conditioned by their diameter as measured $x = 10$ mm in Fig. 1.

a higher axial velocity than those at the other measurement locations ($r = 3, 7$ mm). This highlights the importance of imposing the laminar velocity profile on the droplets at the point of injection using the Laminar FIM-UR model. Experiments and simulations are generally in good agreement. Nevertheless, it is noted that the measurement location 5 mm downstream and 5 mm radially outwards (Fig.12e), droplets with the smallest diameters have a velocity in the simulations that is noticeably lower than in the experiments (Fig.12b).

It is important to note that the appearance of high velocity, large diameter droplets is conditional on a sufficient number of droplets being injected by FIM-UR. This highlights the importance of using the modified Rosin-Rammler distribution instead of the Rosin-Rammler distribution that does not contain these larger droplets.

4.2.1 PDF double peak origin

To better understand the formation of this double peak shape a simulation was run with a preset Rosin-Rammler distribution optimised to fit the experimental data and injected using the FIM-UR model (black dotted line of Fig. 15a). In this simulation, the evaporation model was turned off. Doing so, it would be expected

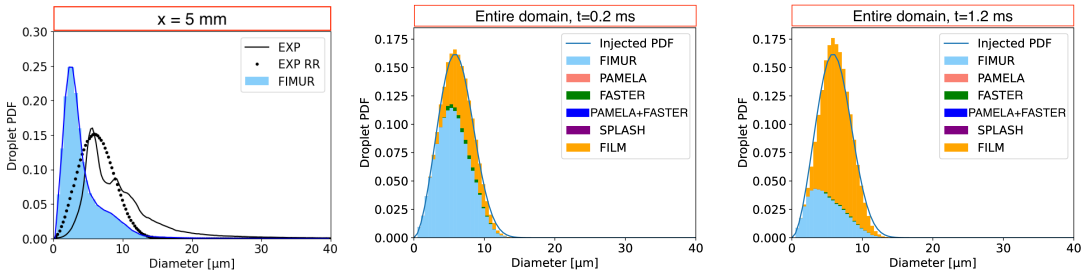

(a) (b) (c)

Fig. 15 The probability of droplets having a certain diameter taken at a plane $x = 5$ mm in Fig. 1 throughout the simulation (a), over the entire domain at $t = 0.2$ ms after the first injection (b) and over the entire domain $t = 1.2$ ms after the first injection (c).

that the distribution retrieved downstream accurately resembles the injected distribution, and therefore the experimental observations. Figure 15a shows this is not the case: there are significantly more droplets in the smaller diameter range than the larger ones arriving at the measurement plane 5 mm downstream of the injector exit and the two peak distribution is clearly visible. Figures 15b and 15c show the distribution given by all of the droplets in the domain at two time instants after the injection begins. As time progresses, the proportion of droplets which are being tracked in the freestream is dropping, meanwhile the number of droplets that are treated as being part of the 'FILM' on the inner surface of the injector is increasing. The distribution of the droplets being absorbed by the FILM is not uniform and is instead skewed with a mean around 7-8 microns. This indicates that the double peak of the downstream distribution is caused by droplets that fall within a certain size range being preferentially absorbed into the liquid film.

This is caused by a "centrifuging" effect: the largest droplets, with a large Stokes number (Stk= τ_p/τ_g is the ratio of the droplet relaxation time to a characteristic time in the gaseous phase), are not greatly affected by the surrounding air-flow and instead travel in a nearly ballistic path radially outwards from the central injector. On the contrary, the smallest droplets, characterised by a very small Stokes number, follow the airflow very closely. As most air does not make contact with the walls of the injector, these droplets do not end up in the film. For droplets between these extremes, they begin to accelerate up to the speed of the swirling flow, however, as their density is much higher than the surrounding air, they begin to be centrifuged out of the air and onto the inside surface of the injector to be enveloped by the film.

4.3 Reacting case

Once validated under cold conditions, the same injection parameters are used in the reactive flow simulation. The droplet diameter PDFs at $x = 5$ and $x = 10$ mm are shown in Figs.16a and 16d respectively. The comparison against the experimental profiles with combustion is very good in both cases. The mean diameter and SMD

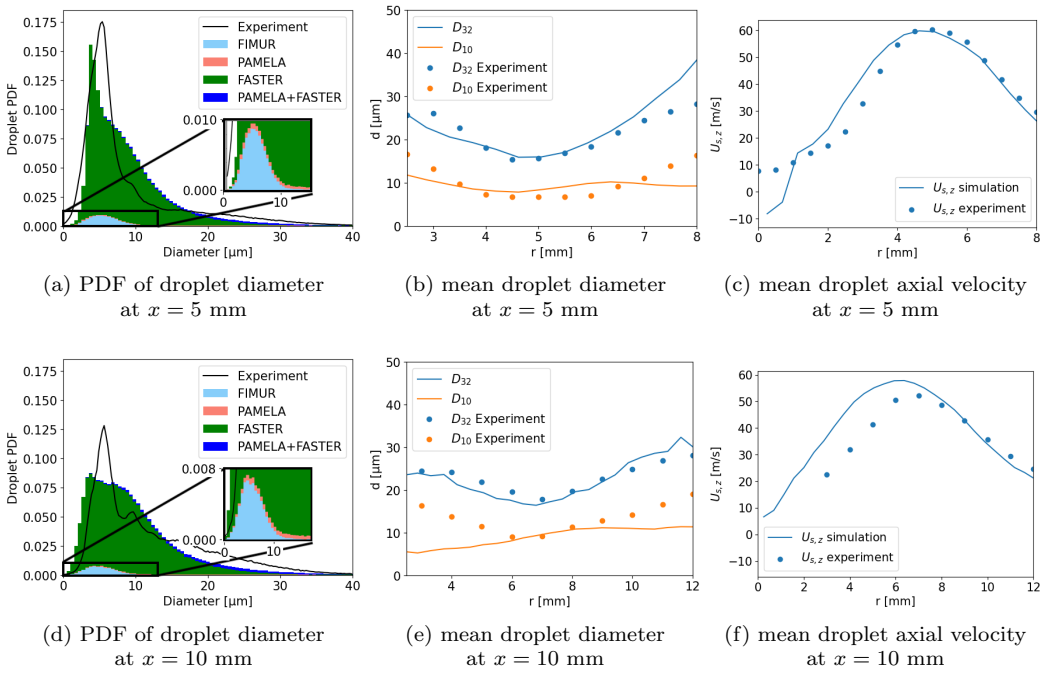

(a) PDF of droplet diameter at $x = 5$ mm

(b) mean droplet diameter at $x = 5$ mm

(c) mean droplet axial velocity at $x = 5$ mm

(d) PDF of droplet diameter at $x = 10$ mm

(e) mean droplet diameter at $x = 10$ mm

(f) mean droplet axial velocity at $x = 10$ mm

Fig. 16 Reactive case: (a-f) as labelled in Fig.11

profiles are shown in Figs.16b and 16e. Unlike in the cold case, the SMD profile matches the experimental values almost perfectly at the 5 mm downstream plane. The velocity profiles shown in Fig.16c show very good agreement with experiment except in the innermost region were the droplet count is very low and the errors high. Further downstream (Fig. 16f) the axial mean velocity shows more deviation from the experimentally measured values on the inner half of the profile.

The conditional probability histograms at $x = 5$ mm downstream are shown in Fig. 17. The experimental histograms (Figs. 17a-c) show a clear deviation from the cold flow (Figs. 12a-c). The two different velocity branches (35 m/s and 10 m/s) are more clearly pronounced in this case and the higher velocity branch is stronger in the reacting case than in the non-reacting. In comparison with simulation values (Fig.17e) at $r = 5$ mm, the experimental histograms are similar but do not show such a strong lower velocity branch (Fig. 17b). The lower velocity branch (around 10 m/s) is also dominant at the 7 mm radial location in the simulations (Fig.17f) but totally absent in the experiment (Fig.17c). This is most likely due to droplets that are atomised by the airblast atomiser being preheated by the hot injector wall during experiments, leading to more rapid evaporation. This effect is not captured in the simulations as heat transfer to the liquid film is not considered in the model. Despite the differences between simulation and experiment, the existence of a higher velocity branch in Fig.17e is only possible thanks to the use of the MRR distribution for the FIM-UR injection and a minimum injection angle which broadens the injection cone. Without the use of the MRR distribution the only large droplets to reach the measurement plane are released by the PAMELA model

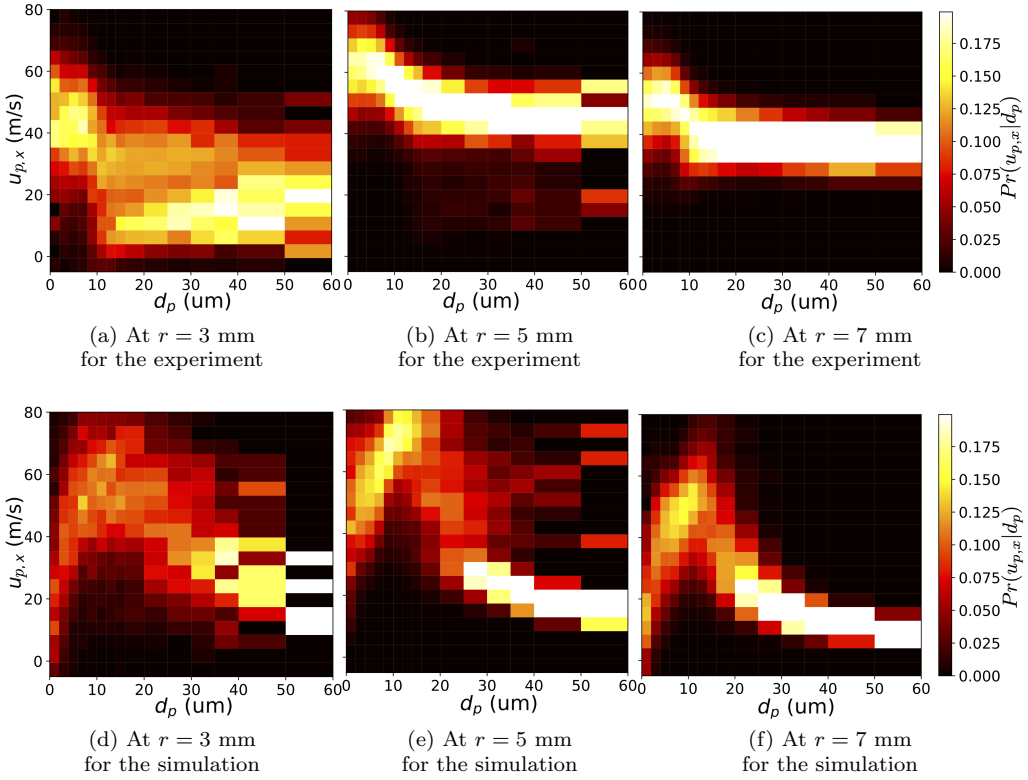

(a) At $r = 3$ mm for the experiment
(b) At $r = 5$ mm for the experiment
(c) At $r = 7$ mm for the experiment
(d) At $r = 3$ mm for the simulation
(e) At $r = 5$ mm for the simulation
(f) At $r = 7$ mm for the simulation

Fig. 17 The probability of droplets having a certain axial velocity ($u_{s,x}$), conditioned by their diameter as measured at $x = 5$ mm in Fig. 1.

which, due to the zero injection velocity, can only contribute to the low velocity branch. Fig. 18 shows the same histograms for the plane 10 mm downstream. In this case, the agreement is good except for more droplets appearing in the high velocity (50 m/s) branch 7 mm radially outwards from the centre in the experiment (Fig. 18c) and slightly more droplets appearing in the low velocity branch (20 m/s) for the simulation (Fig. 18e).

Figure 19 shows the result of OH* measurements of the reacting experimental rig and heat release measurements from the simulation. The M-shaped turbulence spray flame can be seen to have an extremely similar stand-off height between the simulations and experiment and a similar length. Most heat release is found in the two outer lobes of the flame instead of the central region.

5 Conclusion

In conclusion, models required to describe the atomisation processes of a fuel spray in a swirled, air-blasted injector using a Lagrangian formulation for the liquid fuel have been developed, tested and optimised to represent a turbulent swirl spray flame inside an academic test rig (EM2C, CentraleSupelec). These models include

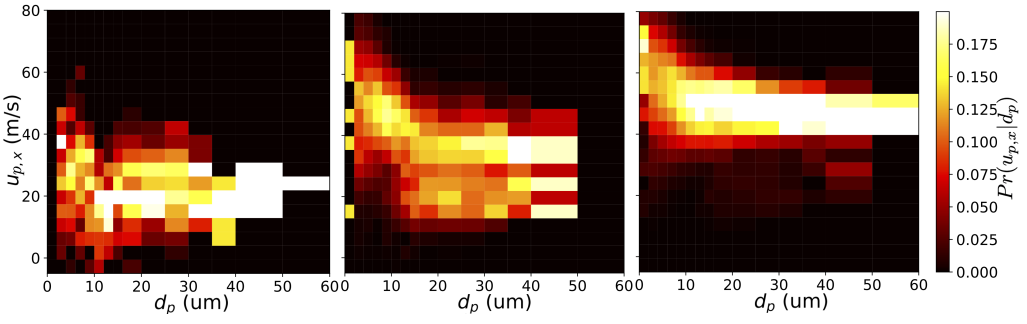

(a) At $r = 3$ mm for the experiment (b) At $r = 5$ mm for the experiment (c) At $r = 7$ mm for the experiment

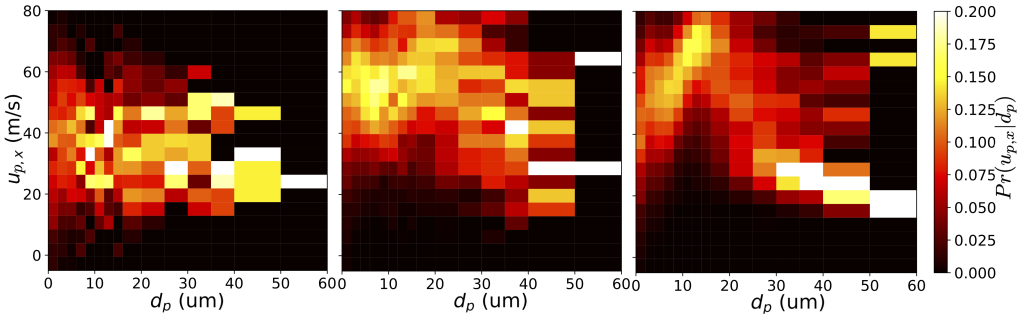

(d) At $r = 3$ mm for the simulation (e) At $r = 5$ mm for the simulation (f) At $r = 7$ mm for the simulation

Fig. 18 The probability of droplets having a certain axial velocity ($u_{s,x}$), conditioned by their diameter as measured at $x = 10$ mm in Fig. 1.

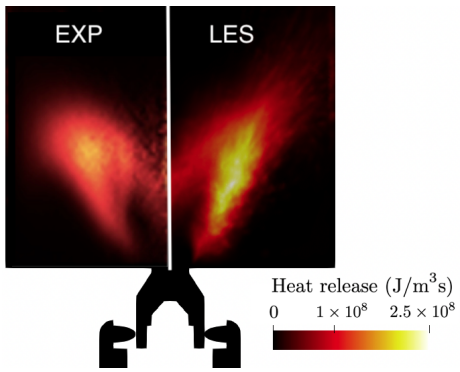

Fig. 19 The mean OH* measurements from the experiments and the mean heat release field from the LES.

the primary atomisation at the pressure-swirl injector, a film model when droplets impact the inner walls of the swirler film and are again atomised at the swirler lips, as well as a secondary atomisation model when droplets propagate in the chamber and in the swirler. Comparisons have been made of the spray statistics downstream of the fuel injector under non-reacting and reacting conditions showing a good agreement with experimental measurements. The comparison of the mean flame shape also agrees with experimental flame visualisation.

An unusual shape of the droplet diameter PDF measured downstream of the injector lips has been shown to be due the centrifuging of droplets of a particular size in the swirling flow inside the fuel injector. A sensitivity analysis has shown that the controlling model parameters are the injection parameters of the FIM-UR model used for the pressure swirl atomiser: the spray angle and the diameter of the injector are the key parameters controlling the rate at which droplets breakup. They also determine the quantity of droplets that exit the injector without filming on the injector walls.

Future work will focus on improvements to the thermal modelling of the liquid film and its relationship to the droplet statistics downstream of the injector and the flame shape. Self-excited thermoacoustic instabilities in the SICCA-Spray and MICCA [58] rigs will also be studied.

Acknowledgements

The authors wish to thank Guillaume Vignat, Preethi Rajendram Soundararajan, Daniel Durox, Antoine Renaud and Sébastien Candel from EM2C for their help in providing the experimental results used in this study.

A Result sensitivity to modelling

Table 2 List of simulations run to test the effect of different modelling approaches.

Simulation	**Model removed**	**and resplaced by**
A	RR distribution	MRR distribution
B	$\theta_{\min} = 15°$	$\theta_{\min} = 2R_a \tan(\theta_S)/(R_0 + R_a)$
C	Eqn.(4)	Eqn.(3)
D	FASTER	FAST

In order to highlight the importance of the modifications made to the original FIM-UR and FAST models, four additional reacting simulations were run (Tab.2). Three of these simulations focus on the modifications that were made to the FIM-UR model: (A) the use of a modified Rosin-Rammler distribution, (B) the additional of a laminar velocity profile, and (C) the inclusion of a manually set minimum injection angle to broaden the spray cone. The final simulation (D) replaces the FASTER secondary atomisation model with the original FAST formulation. Figure 20 shows the probability density function of the droplet velocity conditioned by the droplet diameter as measured at $x = 5$ mm downstream of the injector plane and at $r = 3$ mm radially outwards from the injector centreline. These figures should be compared to Figs. 17a-d. Each of these four model modifications results in a similar problem: the lack of the very largest droplets at this central location in the domain. In the case of the Rosin-Rammler

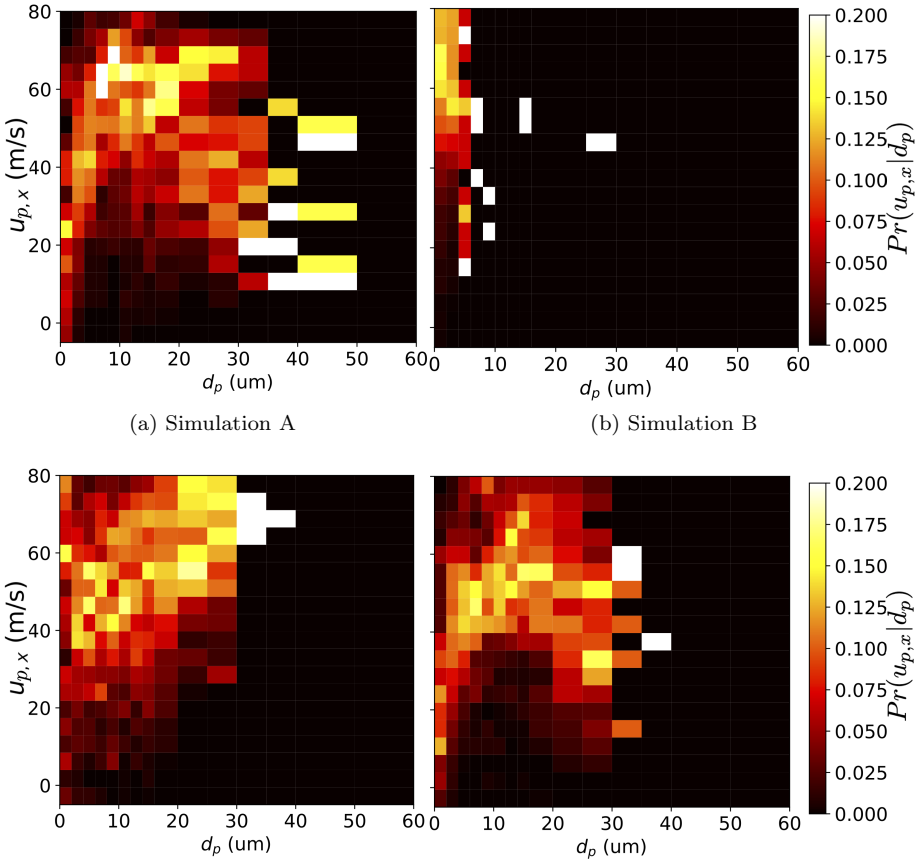

(a) Simulation A (b) Simulation B

(c) Simulation C (d) Simulation D

Fig. 20 The probability of droplets having a certain axial velocity, conditioned by their diameter as measured 5 mm downstream of the exit of the injector and at a radial location of 3 mm from the center of the jet for 4 different simulations.

distribution, the lack of a long *tail* in this distribution means that the small number of very large droplets created by the atomiser is not captured resulting in an overall shift to smaller droplet diameters downstream of the injector. The largest difference is seen in the case of the minimum spray angle being set automatically by FIM-UR: in this case, the only droplets that can reach the central region of the domain are those with very low Stokes numbers as no droplets that are injected directly from the pressure-swirl atomiser can reach the combustion chamber without undergoing breakup or impacting the injector wall. The injection of the droplets with a flat velocity profile equal to the bulk velocity results in the largest observed droplets having too high a velocity at this measurement location and, due to their higher velocity, these droplets breakup too quickly leading to a smaller maximum observed size. As explained in Section 3.2.4, the original FAST model uses a breakup timescale that is too small for low Weber number cases such as in the current study. Figure 20d shows that the effect of this timescale being too small is that droplets breakup too quickly leading to a lack of larger sized droplets at the measurement plane. A comparison between Figures 20 and 17 evidences the improvement resulting from the proposed formulations of FIM-UR and FASTER.

These effects are also highlighted in the measurements of SMD and droplet mean diameter as shown in Fig.21, which can be compared to Fig.16b. This figure shows that the reduction

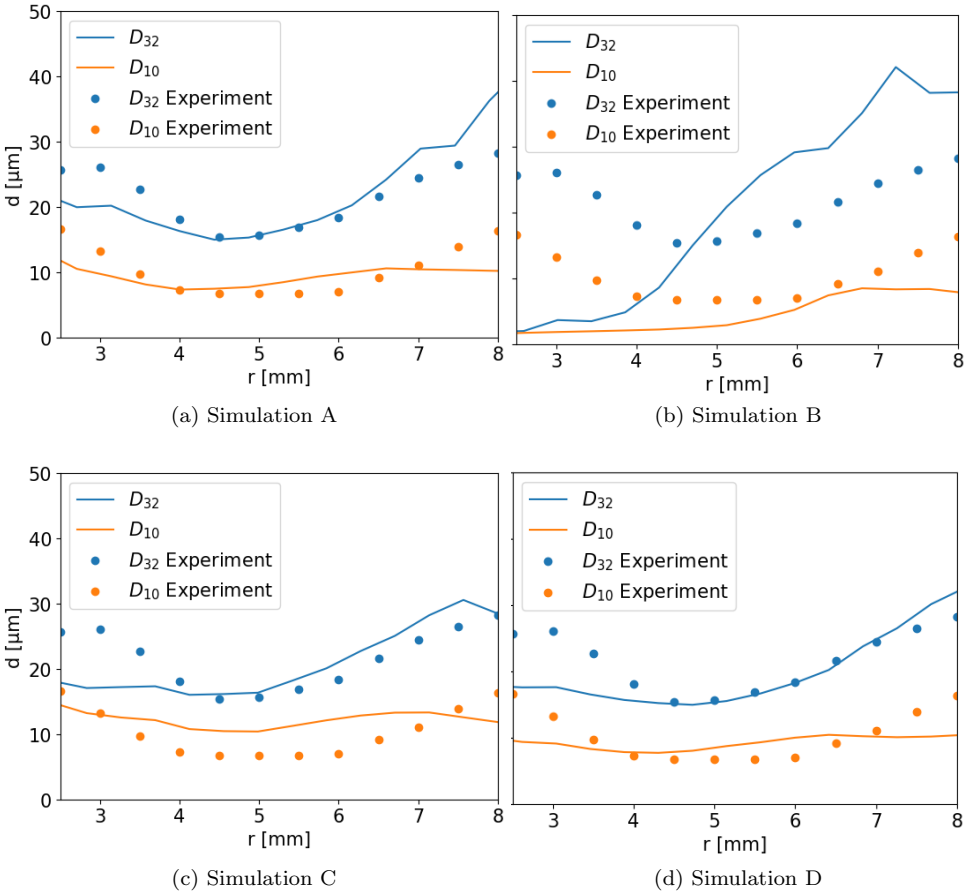

(a) Simulation A (b) Simulation B

(c) Simulation C (d) Simulation D

Fig. 21 The mean droplet diameter and SMD as a function of radial measurement location as measured 5 mm downstream for 4 different simulations.

in the maximum observable droplet size at r=3 mm translates into a corresponding drop in the SMD (and in some cases the mean droplet diameter) close to the centreline of the domain. It is also observable that in the cases of the use of the RR distribution and the change in minimum spray angle, that the SMD is too high at r=8 mm. This may be due to a higher proportion of droplets hitting the injector walls, leading to an increase in the thickness of the liquid film and a corresponding increase in the mean diameter generated by the PAMELA airblast atomisation model.

B Result sensitivity to input parameters

Table 3 gives an estimate of the sensitivity of the model parameters for the four models presented in this study. By far the most sensitive of the models is FIM-UR, in which the injector diameter (D_{ps}), and the angles of injection (θ_S, $\theta_{\min}$) are specified, consequently defining the initial velocity of the droplets. This determines: (1) the speed at which the droplets breakup through the secondary breakup model (FASTER); (2) the proportion of droplets that land on the injector inner surface to be reatomised by the airblast atomiser; and (3) the velocity and physical position of larger droplets measured further downstream. The results are less sensitive

Table 3 List of model parameters, constants and their sensitivity with respect to the final solution.

	Constants	**Parameters**	**Sensitivity**
Laminar FIMUR			
SMD		D_{32}	Medium
Spreading parameter		q	Medium
Mean spray angle		θ_S	High
Minimum spray angle		$\theta_{\min}$	High
Atomiser diameter		$D_{\rm ps}$	High
Velocity variance		σ_u	Low
Automatic PAMELA			
Atomiser thickness		$h_{\rm a}$	High
Model Constants	$C_1 - C_5$		
FILM			
None			
FASTER			
Mean constant		k_1	Low
Variance constant		k_2	Low

to the chosen diameter PDF to be injected: any over-injection of droplets of the smallest size will lead to a reduction in the quality of the observed droplet diameter PDF. On the other hand, an SMD that is too big will result in a more modest change in observed PDF because most large droplets are in both cases broken up by the secondary breakup model. For the spreading parameter (q) it is very important to choose something that does not lead to small sized droplets being generated (i.e. $q > 2$ for the Rosin-Rammler distribution) avoiding on the other hand the injection of a very narrow PDF.

To highlight these sensitivities, the PDF of four different simulations are provided in Fig.22. In Figure 22a, the droplets are injected at a mean injection angle of 30 degrees, from an injector 80 microns wide, with droplets of a uniform diameter of 18 microns. The shallow injection angle reduces the velocity of the droplets leading to less breakup by the secondary breakup model and a PDF that is too wide. The original diameter of the injected particles also appears as a single, unrealistic peak in the PDF. Figure 22b shows a simulation with a mean injection angle of 60 degrees, (the minimum injection angle is calculated by the FIM-UR model in this case) and from an injector with a diameter of 80 microns. This choice of injection angle leads to a droplet velocity that is too high, which causes too much breakup from the secondary breakup model and a PDF that is too thin.

Results are less sensitive to other model parameters. The Automatic PAMELA model has only one sensitive parameter (the prefilmer thickness). The FILM model has no tunable parameters and the FASTER model, while it does allow for some tuning to be made by the user, is relatively insensitive to this choice. In all simulations run in this study the value of $k_1 = 0.8$ is fixed; in one simulation, the value was changed to $k_1 = 1.6$. Figures 22c-d shows that there is almost no change in the observed downstream PDF. This is because the model considers the droplet breakup as a process cascade that occurs many times over. Changing the value of the two constants may change the outcome of one breakup event in this cascade but the droplet will remain unstable as long as the Weber number remains higher than the critical Weber number leading to the same end result. It should be noted that it is possible to change the observed PDF by choosing a k_1 far from unity (as suggested by Apte et al. [44]).

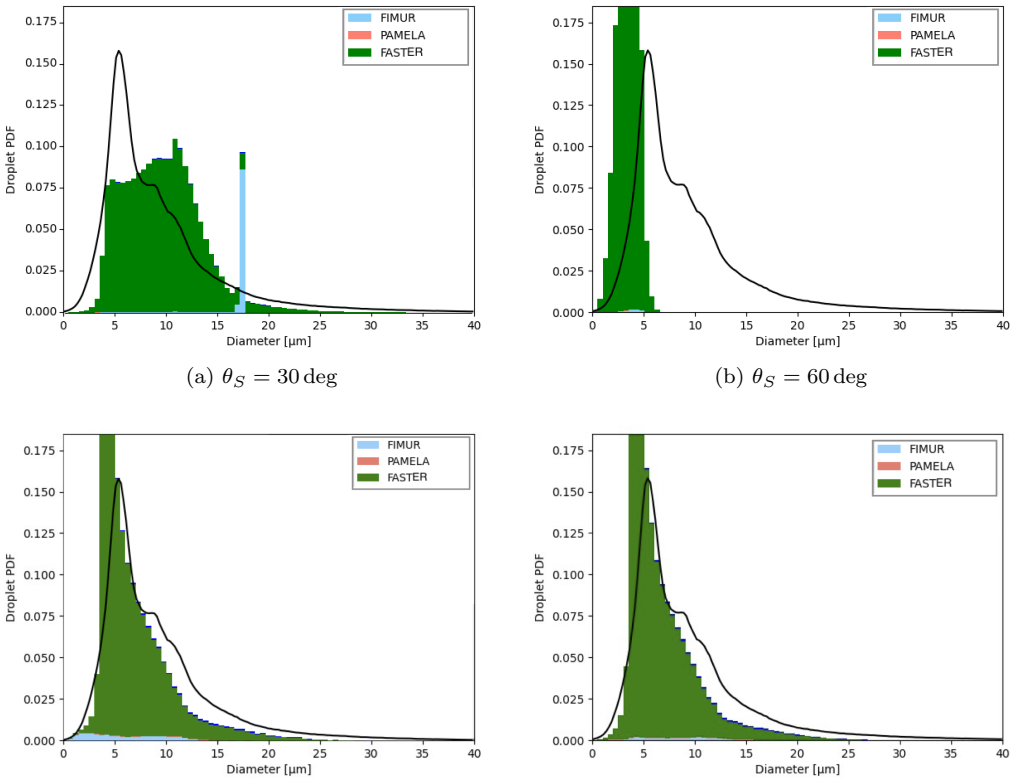

(a) $\theta_S = 30\,\text{deg}$ (b) $\theta_S = 60\,\text{deg}$

(c) $k_1 = 0.8$ (d) $k_1 = 1.6$

Fig. 22 The probability of droplets having a certain diameter as measured 5 mm downstream of the exit of the injector in simulations where the values of the mean spray angle (θ_S) and the first FASTER coefficient (k_1) were varied.

C Ethical Statement

Funding

This work was granted access to the HPC resources of IDRIS under the allocation 2022-[A0112B10157] made by GENCI. This project has received funding from the Clean Sky 2 Joint Undertaking (JU) under grant agreement No. 886554. The JU receives support from the European Union's Horizon 2020 research and innovation programme and the Clean Sky 2 JU members other than the Union. All authors are recipients of this funding.

Conflict of Interest

The authors have no relevant financial or non-financial interests in any material discussed in this article, nor any competing interests to disclose. All authors certify that they have no affiliations with, or involvement in, any organisation or entity with any non-financial or financial interest in the subject matter discussed in this manuscript.

Ethical approval

This research did not involve human or animal subjects. There are no ethical issues.

Informed consent

This research did not involve any human subjects. There are no issues regarding informed consent.

Author contribution

N.T. wrote the manuscript, performed the simulations and prepared the figures, D.L., J.C., N.O., and T.P. edited the manuscript. D.L. also provided the original simulation case files and experimental data (from EM2C). Y. G., J.D., G.D, and L.G. were involved at a project level.

References

1. K. Warncke, S. Gepperth, B. Sauer, A. Sadiki, J. Janicka, R. Koch, and H.-J. Bauer, "Experimental and numerical investigation of the primary breakup of an airblasted liquid sheet," *International Journal of Multiphase Flow*, vol. 91, pp. 208–224, 2017.
2. J. R. Wetherell, A. Garmory, and M. Skarysz, "Coupled level set volume of fluid simulations of prefilming airblast atomization with adaptive meshing," in *Turbo Expo: Power for Land, Sea, and Air*, vol. 84126, p. V04AT04A006, American Society of Mechanical Engineers, 2020.
3. J. Carmona, N. Odier, O. Desjardins, B. Cuenot, A. Misdariis, and A. Cayre, "A comparative study of direct numerical simulation and experimental results on a prefilming airblast atomization configuration," *Atomization and Sprays*, vol. 31, no. 8, 2021.
4. M. Dianat, M. Skarysz, and A. Garmory, "A coupled level set and volume of fluid method for automotive exterior water management applications," *International Journal of Multiphase Flow*, vol. 91, pp. 19–38, 2017.
5. N. Treleaven, A. Garmory, and G. Page, "The effects of turbulence on jet stability and the flame transfer function in a lean-burn combustor," *Combustion Science and Technology*, vol. 192, no. 11, pp. 2115–2137, 2020.
6. W. Jones, A. Marquis, and K. Vogiatzaki, "Large-eddy simulation of spray combustion in a gas turbine combustor," *Combustion and flame*, vol. 161, no. 1, pp. 222–239, 2014.
7. A. Giusti and E. Mastorakos, "Detailed chemistry les/cmc simulation of a swirling ethanol spray flame approaching blow-off," *Proceedings of the Combustion Institute*, vol. 36, no. 2, pp. 2625–2632, 2017.
8. S. Tachibana, K. Saito, T. Yamamoto, M. Makida, T. Kitano, and R. Kurose, "Experimental and numerical investigation of thermo-acoustic instability in a liquid-fuel aero-engine combustor at elevated pressure: Validity of large-eddy simulation of spray combustion," *Combustion and Flame*, vol. 162, no. 6, pp. 2621–2637, 2015.
9. M. Sanjosé, J. Senoner, F. Jaegle, B. Cuenot, S. Moreau, and T. Poinsot, "Fuel injection model for euler–euler and euler–lagrange large-eddy simulations of an evaporating spray inside an aeronautical combustor," *International Journal of Multiphase Flow*, vol. 37, no. 5, pp. 514–529, 2011.
10. J. Su, A. Barker, A. Garmory, and J. Carrotte, "Spray response to acoustic forcing of a multi-passage lean-burn aero-engine fuel injector," in *ASME Turbo Expo 2018*, pp. GT2018–75554, American Society of Mechanical Engineers, 2018.
11. N. C. W. Treleaven, A. Garmory, and G. J. Page, "The effect of sauter mean diameter fluctuations on the heat release rate in a lean-burn aero-engine combustor," in *ASME Turbo Expo 2018*, pp. GT2019–90321, American Society of Mechanical Engineers, 2019.
12. E. Lo Schiavo, D. Laera, E. Riber, L. Gicquel, and T. Poinsot, "Effects of liquid fuel/wall interaction on thermoacoustic instabilities in swirling spray flames," *Combustion and Flame*, vol. 219, pp. 86–101, 2020.

13. S. Puggelli, S. Paccati, D. Bertini, L. Mazzei, A. Giusti, and A. Andreini, "Multi-coupled numerical simulations of the dlr generic single sector combustor," *Combustion Science and Technology*, vol. 190, no. 8, pp. 1409–1425, 2018.
14. G. Vignat, P. Rajendram Soundararajan, D. Durox, A. Vié, A. Renaud, and S. Candel, "A joint experimental and large eddy simulation characterization of the liquid fuel spray in a swirl injector," *Journal of Engineering for Gas Turbines and Power*, vol. 143, no. 8, 2021.
15. E. Lo Schiavo, D. Laera, E. Riber, L. Gicquel, and T. Poinsot, "On the impact of fuel injection angle in euler–lagrange large eddy simulations of swirling spray flames exhibiting thermoacoustic instabilities," *Combustion and Flame*, vol. 227, pp. 359–370, 2021.
16. G. Vignat, D. Durox, K. Prieur, and S. Candel, "An experimental study into the effect of injector pressure loss on self-sustained combustion instabilities in a swirled spray burner," *Proceedings of the Combustion Institute*, vol. 37, no. 4, pp. 5205–5213, 2019.
17. K. Prieur, G. Vignat, D. Durox, T. Schuller, and S. Candel, "Flame and spray dynamics during the light-round process in an annular system equipped with multiple swirl spray injectors," *Journal of Engineering for Gas Turbines and Power*, vol. 141, no. 6, 2019.
18. G. Vignat, E. Lo Schiavo, D. Laera, A. Renaud, L. Gicquel, D. Durox, and S. Candel, "Dynamics of spray and swirling flame under acoustic oscillations: A joint experimental and les investigation," *Proceedings of the Combustion Institute*, vol. 38, no. 4, pp. 6015–6024, 2021.
19. G. Vignat, D. Durox, A. Renaud, T. Lancien, R. Vicquelin, and S. Candel, "Investigation of transient pvc dynamics in a strongly swirled spray flame using high speed planar laser imaging of sno2 microparticles," *Combustion and Flame*, vol. 225, pp. 305–319, 2021.
20. P. Rajendram Soundararajan, D. Durox, A. Renaud, G. Vignat, and S. Candel, "Swirler effects on combustion instabilities analyzed with measured fdfs, injector impedances and damping rates," *Combustion and Flame*, vol. 238, p. 111947, 2022.
21. J.-M. Senoner, *Simulations aux grandes échelles de l'écoulement diphasique dans un brûleur aéronautique par une approche Euler-Lagrange*. PhD thesis, Toulouse, INPT, 2010.
22. G. Chaussonnet, *Modeling of liquid film and breakup phenomena in Large-Eddy Simulations of aeroengines fueled by airblast atomizers*. Theses, Institut National Polytechnique de Toulouse, 2014.
23. G. Chaussonnet, O. Vermorel, E. Riber, and B. Cuenot, "A new phenomenological model to predict drop size distribution in large-eddy simulations of airblast atomizers," *International Journal of Multiphase Flow*, vol. 80, pp. 29–42, 2016.
24. G. Vignat, *Dynamique de L'injection et de la Combustion Dans Des Flammes de Spray Swirlées et Couplage Azimutal Dans Les Foyers Annulaires*. PhD thesis, Université Paris-Saclay, Prepared at CentraleSupélec, Gif-sur-Yvette, France, 2020.
25. N. Gourdain, L. Gicquel, M. Montagnac, O. Vermorel, M. Gazaix, G. Staffelbach, M. Garcia, J. Boussuge, and T. Poinsot, "High performance parallel computing of flows in complex geometries: I. methods," *Computational Science & Discovery*, vol. 2, no. 1, p. 015003, 2009.
26. N. Gourdain, L. Gicquel, G. Staffelbach, O. Vermorel, F. Duchaine, J.-F. Boussuge, and T. Poinsot, "High performance parallel computing of flows in complex geometries - part 2: applications," *Computational Science and Discovery*, vol. 2, no. November, p. 015004, 2009.
27. T. Schønfeld and M. Rudgyard, "Steady and unsteady flow simulations using the hybrid flow solver AVBP," *AIAA Journal*, vol. 37, no. 11, pp. 1378–1385, 1999.
28. O. Colin and M. Rudgyard, "Development of high-order Taylor–Galerkin schemes for LES," *Journal of Computational Physics*, vol. 162, no. 2, pp. 338–371, 2000.
29. O. Colin, "A finite element operator for diffusion terms in AVBP," tech. rep., Institut Français du Pétrole, 2003.
30. F. Nicoud and F. Ducros, "Subgrid-scale stress modelling based on the square of the velocity gradient tensor," *Flow, turbulence and Combustion*, vol. 62, no. 3, pp. 183–200, 1999.
31. G. Daviller, G. Oztarlik, and T. Poinsot, "A generalized non-reflecting inlet boundary condition for steady and forced compressible flows with injection of vortical and acoustic waves," *Computers & Fluids*, vol. 190, pp. 503–513, 2019.
32. T. J. Poinsot and S. Lele, "Boundary conditions for direct simulations of compressible viscous flows," *Journal of computational physics*, vol. 101, no. 1, pp. 104–129, 1992.

33. D. Paulhiac, B. Cuenot, E. Riber, L. Esclapez, and S. Richard, "Analysis of the spray flame structure in a lab-scale burner using large eddy simulation and discrete particle simulation," *Combustion and Flame*, vol. 212, pp. 25–38, 2020.
34. B. Rochette, F. Collin-Bastiani, L. Gicquel, O. Vermorel, D. Veynante, and T. Poinsot, "Influence of chemical schemes, numerical method and dynamic turbulent combustion modeling on les of premixed turbulent flames," *Combustion and Flame*, vol. 191, pp. 417–430, 2018.
35. F. Charlette, C. Meneveau, and D. Veynante, "A power-law flame wrinkling model for les of premixed turbulent combustion part ii: dynamic formulation," *Combustion and Flame*, vol. 131, no. 1-2, pp. 181–197, 2002.
36. H. Yamashita, M. Shimada, and T. Takeno, "A numerical study on flame stability at the transition point of jet diffusion flames," in *Symposium (International) on Combustion*, vol. 26, pp. 27–34, 1996.
37. B. Abramzon and W. Sirignano, "Droplet vaporization model for spray combustion calculations," *International Journal of Heat and Mass Transfer*, vol. 32, no. 9, pp. 1605–1618, 1989.
38. G. Hannebique, P. Sierra, E. Riber, and B. Cuenot, "Large eddy simulation of reactive two-phase flow in an aeronautical multipoint burner," *Flow, Turbulence and Combustion*, vol. 90, no. 2, pp. 449–469, 2013.
39. Z. Naumann and L. Schiller, "A drag coefficient correlation," *Z. Ver. Deutsch. Ing*, vol. 77, no. 318, p. e323, 1935.
40. D. Paulhiac, *Modélisation de la combustion d'un spray dans un brûleur aéronautique*. PhD thesis, INPT, 2015.
41. N. Rizk and A. H. Lefebvre, "Internal flow characteristics of simplex swirl atomizers," *Journal of Propulsion and Power*, vol. 1, no. 3, pp. 193–199, 1985.
42. S. Yoon, J. Hewson, P. DesJardin, D. Glaze, A. Black, and R. Skaggs, "Numerical modeling and experimental measurements of a high speed solid-cone water spray for use in fire suppression applications," *International Journal of Multiphase Flow*, vol. 30, no. 11, pp. 1369–1388, 2004.
43. N. K. Rizk, "Spray characteristics of the LHX nozzle," tech. rep., Allison Gas Turbine Engines Report Nos. AR0300-90 and AR 0300-91, 1984.
44. S. Apte, M. Gorokhovski, and P. Moin, "Les of atomizing spray with stochastic modeling of secondary breakup," *International Journal of Multiphase Flow*, vol. 29, no. 9, pp. 1503–1522, 2003.
45. B. de Saint-Venant, "Théorie du mouvement non permanent des eaux, avec application aux crues de rivières et à l'introduction des marées dans leur lit.," *Comptes Rendus des séances de l'Académie des Sciences*, pp. 147–154, 1871.
46. P. O'rourke and A. Amsden, "A particle numerical model for wall film dynamics in port-injected engines," *SAE transactions*, pp. 2000–2013, 1996.
47. G. Chaussonnet, E. Riber, O. Vermorel, B. Cuenot, S. Gepperth, and R. Koch, "Large eddy simulation of a prefilming airblast atomizer," in *ILASS Europe, Proceedings of the 25th Annual Conference on Liquid Atomization and Spray Systems*, 2013.
48. J. Carmona, *Modélisation des phénomènes diphasiques dans des injecteurs aéronautiques de type Airblast*. PhD thesis, Toulouse, INPT, 2021.
49. J. Carmona, N. C. W. Treleaven, N. Odier, and B. Cuenot, "A lagrangian simulation methodology for prefilming airblast injectors," *Submitted to: the International Journal of Multiphase Flow*, 2022.
50. S. Gepperth, A. Müller, R. Koch, and H. Bauer, "Ligament and droplet characteristics in prefilming airblast atomization," in *12th Triennial International Conference on Liquid Atomization and Spray Systems*, 2012.
51. A. N. Kolmogorov, "On the log-normal distribution of particles sizes during breakup process," in *Dokl. Akad. Nauk. SSSR*, pp. 99–101, 1941.
52. U. Shavit and N. Chigier, "Fractal dimensions of liquid jet interface under breakup," *Atomization and Sprays*, pp. 525–543, 1995.
53. W.-X. Zhou and Z.-H. Yu, "Multifractality of drop breakup in the air-blast nozzle atomization process," *Physical Review E*, vol. 63, no. 1, p. 016302, 2000.
54. R. Brodkey, *The phenomena of fluid motions.* Addison-Wesley, Reading, 1969.
55. M. Pilch and C. Erdman, "Use of breakup time data and velocity history data to predict the maximum size of stable fragments for acceleration-induced breakup of a liquid drop," *International Journal of Multiphase Flow*, vol. 13, no. 6, pp. 741–757, 1987.

56. P. J. O'Rourke and A. A. Amsden, "The tab method for numerical calculation of spray droplet breakup," tech. rep., SAE Technical Paper, 1987.
57. M. Karalus, P. Thakre, G. Goldin, and D. Brandt, "Flamelet Versus Detailed Chemistry LES for a Liquid Fueled Gas-Turbine Combustor: A Comparison of Accuracy and Computational Cost," Turbo Expo 2021, pp. GT2021–59395, 2021.
58. D. Laera, T. Schuller, K. Prieur, D. Durox, S. M. Camporeale, and S. Candel, "Flame describing function analysis of spinning and standing modes in an annular combustor and comparison with experiments," *Combustion and Flame*, vol. 184, pp. 136–152, 2017.